



# Asymptotics of unit Burger number rotating and stratified flows for small aspect ratio

S. Kurien<sup>a,\*</sup>, L.M. Smith<sup>b</sup>

<sup>a</sup> Theoretical Division, Los Alamos National Laboratory, Los Alamos, NM 87501, USA

<sup>b</sup> Departments of Mathematics and Engineering Physics, University of Wisconsin, Madison, WI, USA

## ARTICLE INFO

### Article history:

Available online 30 June 2011

### Keywords:

Rotating flows  
Stratified flows  
Burger number 1 flows  
Small-aspect-ratio flows

## ABSTRACT

Rotating and stably stratified Boussinesq flow is investigated for Burger number unity in domain aspect ratio (height/horizontal length)  $\delta < 1$  and  $\delta = 1$ . To achieve Burger number unity, the non-dimensional rotation and stratification frequencies (Rossby and Froude numbers, respectively) are both set equal to a second small parameter  $\epsilon < 1$ . Non-dimensionalization of potential vorticity distinguishes contributions proportional to  $(\epsilon\delta)^{-1}$ ,  $\delta^{-1}$  and  $O(1)$ . The  $(\epsilon\delta)^{-1}$  terms are the linear terms associated with the pseudo-potential vorticity of the quasi-geostrophic limit. For fixed  $\delta = 1/4$  and a series of decreasing  $\epsilon$ , numerical simulations are used to assess the importance of the  $\delta^{-1}$  contribution of potential vorticity to the potential enstrophy. The change in the energy spectral scalings is studied as  $\epsilon$  is decreased. For intermediate values of  $\epsilon$ , as the flow transitions to the  $(\delta\epsilon)^{-1}$  regime in potential vorticity, both the wave and vortical components of the energy spectrum undergo changes in their scaling behavior. For sufficiently small  $\epsilon$ , the  $(\delta\epsilon)^{-1}$  contributions dominate the potential vorticity, and the vortical mode spectrum recovers  $k^{-3}$  quasi-geostrophic scaling. However, the wave mode spectrum shows scaling that is very different from the well-known  $k^{-1}$  scaling observed for the same asymptotics at  $\delta = 1$ . Visualization of the wave component of the horizontal velocity at  $\delta = 1/4$  reveals a tendency toward a layered structure while there is no evidence of layering in the  $\delta = 1$  case. The investigation makes progress toward quantifying the effects of aspect ratio  $\delta$  on the  $\epsilon \rightarrow 0$  asymptotics for the wave component of unit Burger number flows. At the lowest value of  $\epsilon = 0.002$ , it is shown that the horizontal kinetic energy spectral scalings are consistent with phenomenology that explains how linear potential vorticity constrains energy in the limit  $\epsilon \rightarrow 0$  for fixed  $\delta$ .

Published by Elsevier B.V.

## 1. Introduction

The Boussinesq approximation is a starting point to describe a fairly broad range of oceanic and atmospheric phenomena, depending on the choice of parameters [1–3]. The current investigation is a fundamental turbulence study in the sense that we address qualitative and quantitative aspects of the rotating Boussinesq equations, rather than attempt to explain a particular geophysical phenomenon. Our approach is based on the foundational work of Kolmogorov, Kraichnan and Yaglom [4–7] in that we are interested in asymptotic regimes in idealized flows with the aim of understanding the physical and spectral space distribution of fundamental quantities such as energy. Focusing on unit Burger number  $Bu = NH/(fL) = 1$ , our study aims to distinguish unit-aspect-ratio flows and small-aspect-ratio flows, where  $f$  is the

Coriolis parameter,  $N$  is the buoyancy frequency,  $H$  ( $L$ ) is the domain height (horizontal length), and  $\delta = H/L$  is the domain aspect ratio. Although geophysical flows are usually confined to small-aspect-ratio domains, idealized numerical studies of the rotating Boussinesq equations are a mix of calculations performed in domains of unit aspect ratio (e.g., [8–15]) and domains of small aspect ratio (e.g., [16,17]).

The nature of turbulence under the influence of rotation and stratification has a long and rich history. As anticipated in [18,19], the strong stratification limit with  $Fr \rightarrow 0$ ,  $Bu \gg 1$  results in a closed, reduced dynamical system involving diffusively coupled, horizontal layers [20,2]. This layering and the formation of the so-called vertically sheared horizontal flow (VSHF) have been systematically observed in decaying [21–23] and forced scenarios [24–27,10]. With large-scale forcing, it is known that  $Bu \gg 1$  flow with finite small  $Fr$  supports a robust forward transfer of energy. This forward transfer is attributed to the “unfreezing” of ageostrophic cascades [28] and has been numerically verified [9–11,29,13]. The scaling of the energy spectrum appears to depend on the nature and dimensionality of the forcing [9,10,29]. The parameter regime of interest here is finite, small  $Fr$  with

\* Corresponding author. Tel.: +505 665 1248.

E-mail addresses: [skurien@lanl.gov](mailto:skurien@lanl.gov) (S. Kurien), [lsmith@math.wisc.edu](mailto:lsmith@math.wisc.edu) (L.M. Smith).

$Bu = 1$ . The limiting dynamics for  $Fr \rightarrow 0$ ,  $Bu = 1$  are described by a different closed, reduced dynamical system known as the quasi-geostrophic (QG) approximation (see [28,30] and further discussion below). The transition between  $Bu \gg 1$  and  $Bu = 1$  for finite, small  $Fr$  in a unit-aspect-ratio domain  $\delta = 1$  was studied numerically in [11].

Our numerical calculations are restricted to the cases  $\delta = 1$  and  $\delta = 1/4$ , with moderate to small values of the Rossby  $Ro = U/(fL)$  and Froude  $Fr = U/(NH)$  numbers  $0.002 \leq Ro = Fr \leq 0.05$ . Here both  $Ro$  and  $Fr$  are based on a velocity scale  $U$  imposed by an external force. For fixed Burger number  $Bu = 1$ , decreasing the domain aspect ratio  $\delta$  requires increasing the ratio  $N/f$ , and we explore the corresponding change in energy spectral scalings and flow structure. In some respects, the  $Bu = 1$ ,  $\delta < 1$  flow resembles flow for  $Bu = 1$ ,  $\delta = 1$  [8], however, other flow features are closer to stratification dominated flow with  $Bu \gg 1$  [27,22,9–11,29,31,32]. It is precisely this dual flow nature that we wish to expose and quantify. For a given aspect ratio  $\delta$ , resolution constraints limit the lower bound for  $Ro = Fr = \epsilon$ . In addition, it is necessary to make specific choices for the external force, grid spacing and dissipation scheme(s). Thus the current study addresses a subset of the possible numerical studies of  $Bu = 1$  flows. In particular, only large-scale forcing is considered and we focus on transfer of energy and potential enstrophy from large to small scales.

The conservation of potential vorticity following fluid particles is an important constraint on rotating and stratified flows in the absence of forcing and dissipation [1–3]. The scalar potential vorticity  $q(\mathbf{x}, t)$  is given by  $q = \omega_a \cdot \nabla \rho_T$ , where  $\omega_a = \omega + f\hat{\mathbf{z}}$  is the absolute vorticity,  $\omega = \nabla \times \mathbf{u}$  is the local vorticity and  $\rho_T$  is the density with fluctuating part  $\rho$ . Conservation of  $q$  following fluid particles means that the component of vorticity along the direction of the density gradient is advected by the flow, but cannot be generated or destroyed. This powerful constraint is fundamental for understanding geophysical flows and is embedded in many models and theoretical analyses. One of the most famous reduced equations used for theoretical and modeling purposes is the QG equation [33]. The QG model describes advection of the linear part of the potential vorticity  $q_{qg} = f\partial\rho/\partial z - N\omega \cdot \hat{\mathbf{z}}$ , called the pseudo-potential vorticity. The direction  $\hat{\mathbf{z}}$  is the rotation axis and the direction of stratification. Conservation of pseudo-potential vorticity  $q_{qg}$  is equivalent to advection of a scalar stream function by the horizontal velocity  $\mathbf{u}_h$  (perpendicular to  $\hat{\mathbf{z}}$ ). Thus large-scale QG dynamics of the horizontal flow and the density fluctuations are determined entirely by a single scalar equation for  $q_{qg}$ , together with an inversion to obtain  $\mathbf{u}_h$  and  $\rho$  from  $q_{qg}$ . The QG structure is similar to two-dimensional Navier–Stokes flow for which the velocity field is given by a single equation for the (scalar) vorticity, or equivalently the stream function.

The QG approximation, reflecting conservation of linear potential vorticity, may be derived in several ways. The more traditional derivation uses a perturbation expansion of the dynamical variables in powers of  $\epsilon$ . Keeping terms to  $O(\epsilon)$ , the QG equation is a solvability condition (see, e.g. [1]). Another way to derive the QG approximation is by projection of the full Boussinesq equations onto the vortical linear eigenmodes [34,12]. There are three types of solutions to the linear, inviscid, unforced Boussinesq equations, which together form an orthogonal basis for the full nonlinear dynamics: two inertia–gravity wave modes with oppositely signed wave frequencies, and the vortical eigenmode with zero frequency [8,2,12]. The decomposition into vortical and wave eigenmodes allows for a convenient formulation of the natural dynamical hierarchy in terms of resonant, near-resonant and non-resonant interactions resulting from the dispersive modulation of the advective nonlinearity [8,12,13]. The QG model is equivalent to nonlinear interactions of the vortical modes in the absence of the inertia–gravity waves. Rigorous theoretical analysis shows that

the evolution of vortical modes is decoupled from inertia–gravity waves in the limit  $Fr = Ro = \epsilon \rightarrow 0$  for  $Bu = 1$  [30,28], thus providing a rigorous foundation for the QG approximation. To describe finite  $\epsilon$  flow, models ‘intermediate’ between QG and the full Boussinesq system have been developed to couple vortical and inertia–gravity modes (see, e.g., [35–40]). Here we also explore  $Bu = 1$  flows at finite  $\epsilon$ , as  $\epsilon$  is decreased for fixed aspect ratio  $\delta = 1/4$ .

We explore approach to the asymptotic regime wherein the potential vorticity approaches its linear part as  $\epsilon$  is decreased, keeping the aspect ratio  $\delta$  fixed and  $Bu = 1$ . Thus the potential vorticity  $q(\mathbf{x}, t)$  and the potential enstrophy  $Q(\mathbf{x}, t) = |q(\mathbf{x}, t)|^2/2$  are used to monitor flow development. From the appropriate non-dimensional expression for  $q$ , one could deduce that, compared to  $\delta = 1$ , smaller values of  $\epsilon$  are necessary for the  $\delta < 1$  case to achieve the asymptotic limit in which linear potential vorticity is dominant. For  $\delta = 1/4$ , we find that  $q$  is dominated by its linear part for  $\epsilon \approx 0.002$ , while quadratic contributions remain important for larger values of  $\epsilon$ . In contrast, for  $\delta = 1$ , we have observed that  $\epsilon \approx 0.007$  is sufficiently small to enable near-asymptotic behavior of  $q$  and  $Q$  (see data for larger  $\epsilon$  reported in [14]) and the well-known scalings of the energy spectra; indeed decreasing  $\epsilon$  further for  $\delta = 1$  does not appear to change the qualitative (visual) or quantitative (spectral) behavior of the flow. For  $\delta = 1$  and  $\delta = 1/4$ , we compare the contribution from inertia–gravity waves with  $Bu = 1$  and  $\epsilon \approx 0.002$ . We emphasize that the comparison makes sense because, in both cases,  $\epsilon$  is small enough so that potential vorticity  $q$  is dominated by its linear part, and thus an asymptotic regime in  $q$  has been achieved. Since  $N/f = 4$  for  $\delta = 1/4$ , the wave component of the flow shows more tendency for horizontal layering than for  $N = f$  and  $\delta = 1$ . While the corresponding wave mode energy spectrum scales as  $k^{-1}$  for  $\delta = 1$  [8], the wave mode energy spectrum we here compute for  $\delta = 1/4$  is steeper, thus associated with larger-scale structures. As  $\epsilon$  is decreased from  $\epsilon = 0.05$  to  $\epsilon = 0.002$ , the total and wave mode spectra exhibit tendencies toward dual scaling in wavenumber  $k$  with transition from steep to shallower scaling. These dual scaling regimes in  $k$  for the wave mode spectra are shown to arise from dominant scaling in vertical wavenumber  $k_z$  rather than horizontal wavenumber  $k_h$ .

Our simulations are most closely related to the rotating Boussinesq simulations of [8,11,13–16], but with different focus. In [16], the primary goal was to investigate the atmospheric spectrum [41], with an attempt to match tropospheric parameters as closely as possible including the small-aspect-ratio domain. The others [8,11,13–15] are all numerical studies in a unit-aspect-ratio domain. The investigation [8] is a benchmark study of geostrophic adjustment in decaying flow with  $Bu = 1$ , showing the spectral scalings  $k^{-3}$  and  $k^{-1}$  of high wavenumber vortical and wave modes, respectively. Further, [8] explains the role of catalytic wave–vortical-wave interactions for the forward cascade of wave energy and associated  $k^{-1}$  spectrum. The later work [11] characterizes the transition from QG-like flow with  $Bu = 1$  to stratified turbulence with  $Bu \gg 1$ . The simulations in [13] contrasted  $Bu = 1$  ( $N = f$ ) flow with stratification dominated flows ( $1 < N/f \leq 5$ ) and rotation dominated flows ( $1 < f/N \leq 5$ ). The numerical work [13] supports the analytical prediction [28] for qualitatively different contributions from the catalytic interactions in the regimes  $Bu \gg 1$  and  $Bu \ll 1$ . In [14,15], it is shown how the forward cascade of potential enstrophy constrains the scalings of potential and kinetic energy spectra, in rotation and/or stratification dominated regimes.

In contrast to the aforementioned studies [8,11,13–16], our purpose here is to begin a systematic comparison of  $Bu = 1$  flows in unit- and small-aspect-ratio domains. The most pronounced difference is in the scaling of the wave mode spectrum for  $\delta = 1/4$  as compared to the case  $\delta = 1$ . On the other hand, the

vortical mode spectra at both aspect ratios recovers 3DQG scaling of  $k^{-3}$ . For  $\delta = 1/4$ , we also explore the transitions in spectral scalings as  $Ro = Fr = \epsilon$  is decreased to sufficiently small values such that potential vorticity is dominated by its linear piece. The calculations we present required approximately 25 million processor hours on the IBM Blue Gene/P supercomputer at Argonne National Laboratory, and a further allocation is necessary to expand the study. At present one can only speculate that further reducing  $\epsilon < 0.002$  would not lead to changes in structure and spectral scaling behavior of the wave modes, since the regime of linear potential vorticity has been achieved. It also remains to systematically investigate smaller values of the aspect ratio  $\delta$ .

The remainder of the manuscript is organized as follows. Section 2 reviews the governing equations and the non-dimensional expressions for potential vorticity and potential enstrophy. Section 3 discusses our numerical procedure to solve the rotating Boussinesq equations, our choices for forcing and dissipation schemes and defines some of the post-processing spectral and physical space diagnostics used to analyze the data. The results of numerical simulations are presented and discussed in Section 4. A summary is given in Section 5.

## 2. Equations of motion

The dimensional Boussinesq equations for stably stratified flow in a rotating frame are given by

$$\frac{D}{Dt} \mathbf{u} + f \hat{\mathbf{z}} \times \mathbf{u} + \frac{1}{\rho_0} \nabla p + \frac{\rho}{\rho_0} g \hat{\mathbf{z}} = \nu \nabla^2 \mathbf{u}, \quad (1)$$

$$\frac{D}{Dt} \rho - b(\mathbf{u} \cdot \hat{\mathbf{z}}) = \kappa \nabla^2 \rho, \quad \nabla \cdot \mathbf{u} = 0, \quad (2)$$

where  $D/Dt = \partial/\partial t + \mathbf{u} \cdot \nabla$  is the derivative following fluid particles and  $\hat{\mathbf{z}}$  is the rotation axis as well as the direction of stratification. Eqs. (1)–(2) follow from conservation of mass, momentum and energy [1–3], where the dynamical variables are the velocity  $\mathbf{u}(\mathbf{x}, t)$ , the effective pressure  $p(\mathbf{x}, t)$  and the fluctuating part of the density  $\rho(\mathbf{x}, t)$ . The total density  $\rho_T(\mathbf{x}, t)$  has been decomposed as  $\rho_T(\mathbf{x}, t) = \rho_0 - bz + \rho(\mathbf{x}, t)$ , where  $\rho_0$  is constant,  $b$  is also constant and larger than zero for stable stratification, and assumptions underlying the Boussinesq approximation are  $|\rho| \ll |bz|$ , and  $|\rho| \ll \rho_0$  with background in hydrostatic balance  $\rho_0 g = \partial p_0 / \partial z$ . For some geophysical flows, it is more appropriate to expand around a background potential temperature instead of density [42] but the form of the equations remains the same. The dimensional parameters defining (1)–(2) are the Coriolis parameter  $f = 2\Omega$ , the buoyancy frequency  $N = (gb/\rho_0)^{1/2}$ , the acceleration of gravity  $g$ , the kinematic viscosity  $\nu$  and the thermal diffusivity  $\kappa$ . Our simulations will be done in a periodic domain, with constant  $f$  and  $N$ .

For an unbounded or periodic domain, the linear eigenmodes of (1)–(2) are Fourier modes such that  $[\mathbf{u}(\mathbf{x}, t); \rho(\mathbf{x}, t)] = \boldsymbol{\phi}^m(\mathbf{k}) \exp[i(\mathbf{k} \cdot \mathbf{x} - \sigma_m(\mathbf{k})t)]$  with four-component basis vector  $\boldsymbol{\phi}^m(\mathbf{k}, t) = [\tilde{\mathbf{u}}^m(\mathbf{k}, t); \tilde{\rho}^m(\mathbf{k}, t)]$ . There are three types of eigenmodes corresponding to  $m = 0, \pm 1$ : the non-wave vortical modes  $\boldsymbol{\phi}^0(\mathbf{k})$  with  $\sigma_0(\mathbf{k}) = 0$ ; and two wave modes  $\boldsymbol{\phi}^\pm(\mathbf{k})$  with wave frequency  $\sigma(\mathbf{k})$  given by the dispersion relation

$$\sigma_\pm(\mathbf{k}) = \pm \frac{(N^2 k_h^2 + f^2 k_z^2)^{1/2}}{k} \quad (3)$$

where  $k_h = (k_x^2 + k_y^2)^{1/2}$  is the horizontal wavenumber. The eigenfunctions themselves are well known (see e.g. [12]) and are given in the Appendix. The linearized equations conserve the linear part of the potential vorticity  $q_{qg} = f \partial \rho / \partial z - N \boldsymbol{\omega} \cdot \hat{\mathbf{z}}$ , which is associated entirely with the vortical modes  $\boldsymbol{\phi}^0(\mathbf{k})$ .

The linear eigenmodes serve as a useful orthogonal and complete basis to represent the solution to the full nonlinear equations. The decomposition

$$\begin{aligned} \boldsymbol{\phi}(\mathbf{k}, t) &= [\tilde{\mathbf{u}}(\mathbf{k}, t); \tilde{\rho}(\mathbf{k}, t)] \\ &= \sum_{m=0,\pm} b_m(\mathbf{k}, t) \boldsymbol{\phi}^m(\mathbf{k}, t) \exp[i(\mathbf{k} \cdot \mathbf{x} - \sigma_m(\mathbf{k})t)] \end{aligned} \quad (4)$$

diagonalizes the linear part of (1)–(2), where the amplitudes  $b_m(\mathbf{k}, t)$  are now the unknowns to be determined. In Fourier space, (1)–(2) (inviscid for simplicity) become

$$\frac{db_m(\mathbf{k}, t)}{dt} = \sum_{\mathbf{k}=\mathbf{p}+\mathbf{q}} \sum_{n,l} C_{\mathbf{k}\mathbf{p}\mathbf{q}}^{mnl} b_n(\mathbf{p}, t) b_l(\mathbf{q}, t) e^{i(\sigma_m(\mathbf{k}) - \sigma_n(\mathbf{p}) - \sigma_l(\mathbf{q}))t} \quad (5)$$

where  $\mathbf{k}$  is discrete in (5) and nonlinear interactions are among triads with  $\mathbf{k} = \mathbf{p} + \mathbf{q}$ . The coupling coefficient  $C_{\mathbf{k}\mathbf{p}\mathbf{q}}^{mnl}$  is calculated explicitly from the eigenmodes  $\boldsymbol{\phi}^m(\mathbf{k})$ :

$$C_{\mathbf{k}\mathbf{p}\mathbf{q}}^{mnl} = \frac{-i}{2} ((\phi_{\mathbf{u}}^n(\mathbf{p}) \cdot \mathbf{q}) \phi^l(\mathbf{q}) + (\phi_{\mathbf{u}}^l(\mathbf{q}) \cdot \mathbf{p}) \phi^n(\mathbf{p})) \cdot (\phi^m(\mathbf{k}))^*, \quad (6)$$

where  $()^*$  denotes the complex conjugate and  $\phi_{\mathbf{u}}^m$  contains the first three components of  $\boldsymbol{\phi}^m$  corresponding to the velocity entries. Notice that, with this symmetric definition,  $C_{\mathbf{k}\mathbf{p}\mathbf{q}}^{mnl} = C_{\mathbf{k}\mathbf{q}\mathbf{p}}^{mln}$ .

Our investigation addresses the forward transfer of energy in (1)–(2) [or equivalently the viscous version of (5)] under the influence of a large-scale, random force in a small-aspect-ratio domain with vertical height  $H$  smaller than its horizontal length  $L$  such that  $H/L = \delta < 1$ . The external force is added to the right hand side of (1)–(2) [or (5) with a viscous term] and will be described in detail below.

For such a flow, an appropriate non-dimensionalization of (1)–(2) scales horizontal distances  $x, y$  by  $L$ , vertical distances  $z$  by  $H$ , and all velocity components by a characteristic large-scale velocity  $U = (\varepsilon/k_f)^{1/3}$ , where the force is localized in wavenumber with associated energy input rate  $\varepsilon$  and peak wavenumber  $k_f$ . Pressure is scaled by  $\rho_0 U^2$  and density fluctuations by  $B \rho_0$  with  $B$  (non-dimensional) constant. Then the non-dimensional form of (1)–(2) is given by

$$\begin{aligned} \frac{D_\delta}{Dt} \mathbf{u} + Ro^{-1} \hat{\mathbf{z}} \times \mathbf{u} + \nabla_\delta p + \gamma \rho \hat{\mathbf{z}} &= Re^{-1} \nabla_\delta \cdot \nabla_\delta \mathbf{u}, \\ \frac{D_\delta}{Dt} \rho - \gamma^{-1} (Fr \delta)^{-2} \rho w &= (Pr Re)^{-1} \nabla_\delta \cdot \nabla_\delta \rho, \quad \nabla_\delta \cdot \mathbf{u} = 0, \end{aligned} \quad (7)$$

where  $D_\delta/Dt = \partial_t + \mathbf{u} \cdot \nabla_\delta$ ,  $\nabla_\delta = \nabla_h + \hat{\mathbf{z}} \delta^{-1} \partial_z$ ,  $\nabla_h = \hat{\mathbf{x}} \partial_x + \hat{\mathbf{y}} \partial_y$  and we have adopted the shorthand notation  $\partial_i$  for the partial derivative with respect to  $i$ . The non-dimensional parameters are the Rossby number  $Ro = U/(fL)$ , the Froude number  $Fr = U/(NH)$ , the aspect ratio  $\delta = H/L$ , the Reynolds number  $Re = UL/\nu$ , the Prandtl number  $\nu/\kappa$  and  $\gamma = BgL/U^2$  with constraint  $\gamma = (\delta Fr)^{-1}$  for conservation of energy. The latter constraint selects the appropriate non-dimensional coefficient  $B$  in terms of the characteristic (imposed) velocity  $U$  by the consistency relation  $B = U(g\rho_0/b)^{-1/2}$ .

As is well known, the inviscid, non-diffusive limit of the Boussinesq equations conserves potential vorticity  $q = (\boldsymbol{\omega} + Ro^{-1} \hat{\mathbf{z}}) \cdot \nabla_\delta \rho_T$  following fluid particles:

$$\frac{D_\delta}{Dt} q = \frac{D_\delta}{Dt} \left( (Ro \delta)^{-1} \partial_z \rho - (Fr \delta)^{-1} \boldsymbol{\omega} \cdot \hat{\mathbf{z}} + \boldsymbol{\omega} \cdot \nabla_\delta \rho \right) = 0, \quad (8)$$

where  $\boldsymbol{\omega}$  is the relative vorticity  $\boldsymbol{\omega} = \nabla_\delta \times \mathbf{u}$  and from now on all flow quantities are non-dimensional. The constant piece of  $q$  (that is,  $Ro^{-1} Fr^{-1}$ ) has been dropped since it does not contribute to the conservation law(s). The linear part  $q_{qg} = (Ro \delta)^{-1} \partial_z \rho - (Fr \delta)^{-1} \boldsymbol{\omega} \cdot \hat{\mathbf{z}}$  is the pseudo-potential vorticity conserved by the quasi-geostrophic equations in the limit  $Ro \sim Fr \rightarrow 0$ . In addition,

**Table 1**  
Some parameters for the numerical simulations of the Boussinesq equations. All simulations were forced with fixed energy input rate  $\varepsilon_f$ , at forcing wavenumber  $k_f = 4\Delta k_z$ , and hyperviscous dissipation with Laplacian to the power 8.

Run #	Grid	$\varepsilon_f$	$\delta = H/L$	$f$	$N$	$\epsilon = Ro = Fr$
1	$512 \times 512 \times 128$	1	0.25	108.1	432.4	0.05
2	$1024 \times 1024 \times 256$	1	0.25	108.1	432.4	0.05
3	$2048 \times 2048 \times 512$	1	0.25	108.1	432.4	0.05
4	$2048 \times 2048 \times 512$	1	0.25	540.5	2162	0.01
5	$2048 \times 2048 \times 512$	1	0.25	1080	4324	0.005
6	$2048 \times 2048 \times 512$	1	0.25	2702.6	10810.3	0.002
7	$1024 \times 1024 \times 256$	1	0.25	2702.6	10810.3	0.002
8	$640 \times 640 \times 640$	0.5	1	3000	3000	0.0023

the domain-averaged energy  $E$  and potential enstrophy  $Q$  are conserved according to

$$\partial_t E = \partial_t \int_D E(\mathbf{x}) \, d\mathbf{x} = \partial_t \int_D \frac{1}{2} (\mathbf{u} \cdot \mathbf{u} + \rho^2) \, d\mathbf{x} = 0 \quad (9)$$

$$\partial_t Q = \partial_t \int_D \frac{1}{2} q^2(\mathbf{x}) \, d\mathbf{x} = 0 \quad (10)$$

where  $\int_D$  indicates integration over the domain.

We focus on Burger unity flows with  $Bu = NH/(fL) = Ro/Fr = 1$ , fixed aspect ratio  $\delta$  and decreasing  $Ro = Fr = \epsilon < 1$ . For compactness, we rewrite

$$\begin{aligned} q &= (\epsilon\delta)^{-1}(\partial_z \rho - \boldsymbol{\omega} \cdot \hat{\mathbf{z}}) + \boldsymbol{\omega} \cdot \nabla_\delta \rho \\ &= (\epsilon\delta)^{-1}a(\mathbf{x}) + \delta^{-1}b(\mathbf{x}) + c(\mathbf{x}), \end{aligned} \quad (11)$$

with definitions

$$\begin{aligned} a(\mathbf{x}) &\equiv (\partial_z \rho - \boldsymbol{\omega} \cdot \hat{\mathbf{z}}), \\ b(\mathbf{x}) &\equiv (\partial_z u \partial_y \rho - \partial_z v \partial_x \rho + (\boldsymbol{\omega} \cdot \hat{\mathbf{z}}) \partial_z \rho), \\ c(\mathbf{x}) &\equiv (\partial_y w \partial_x \rho - \partial_x w \partial_y \rho). \end{aligned} \quad (12)$$

In the numerical computations for fixed  $\delta = 1/4$  and decreasing  $\epsilon$ , we wish to assess the importance of the term  $\delta^{-1}b(\mathbf{x})$  in (11) compared to the linear component  $q_{\text{ag}} = (\epsilon\delta)^{-1}a(\mathbf{x})$ . Directly using  $q$  as a probe poses problems because it is sign-indefinite (noisy) and its global mean is zero for periodic or other boundary conditions without sources at the boundaries. Therefore, we use the global potential enstrophy  $Q$  as a surrogate to monitor for asymptotic regimes in  $q$ . In the data analysis of potential enstrophy  $Q$ , we compare

$$Q = \frac{1}{2} \int_D q^2 \, d\mathbf{x}, \quad (13)$$

$$Q_{[\epsilon\delta, \delta]} \equiv \frac{1}{2} \int_D \left( (\epsilon\delta)^{-1}a + \delta^{-1}b \right)^2 \, d\mathbf{x}, \quad (14)$$

and

$$Q_{[\epsilon\delta]} \equiv \frac{1}{2} \int_D (\epsilon\delta)^{-2} a^2 \, d\mathbf{x}. \quad (15)$$

The subscript  $[\epsilon\delta, \delta]$  is used to distinguish the contribution to potential enstrophy from  $q \sim (\epsilon\delta)^{-1}a(\mathbf{x}) + \delta^{-1}b(\mathbf{x})$ . The subscript  $[\epsilon\delta]$  is used to distinguish the contribution to potential enstrophy from the asymptotically dominant linear  $q \sim (\epsilon\delta)^{-1}a(\mathbf{x})$ . When  $Q \approx Q_{[\epsilon\delta, \delta]}$ , then quite obviously the  $\delta^{-1}b(\mathbf{x})$ -term remains important in the potential vorticity (11). When  $Q \approx Q_{[\epsilon\delta, \delta]} \approx Q_{[\epsilon\delta]}$ , then the asymptotic quasi-geostrophic regime of linear potential vorticity is approached, that is, the  $\delta^{-1}$  and  $O(1)$  terms in  $q$  become negligible. We study the change in the energy spectra as  $\epsilon$  is decreased and the simulations show transition from an intermediate  $\epsilon$ -regime with  $Q \approx Q_{[\epsilon\delta, \delta]}$  to the asymptotic regime with  $Q \approx Q_{[\epsilon\delta]}$ . As shown in [8,13], the wave mode spectrum scales as  $k^{-1}$  for small enough  $\epsilon$  in a unit-aspect-ratio domain ( $\delta = 1$ ). In contrast, in the small-aspect-ratio domain with  $\delta = 1/4$ , the

wave mode spectrum is steeper, and changes continuously as  $\epsilon$  is decreased from  $\epsilon = 0.05$  to  $\epsilon = 0.002$ . For intermediate values of  $\epsilon$  such that the potential vorticity (11) is a mix of contributions from  $(\epsilon\delta)^{-1}$ -terms and  $\delta^{-1}$ -terms and potential enstrophy is  $Q \approx Q_{[\epsilon\delta, \delta]}$ , then the wave mode spectrum appears to exhibit dual scaling regimes with transition from steep to shallower scaling. Even higher resolutions would be necessary for confirmation of the latter.

### 3. Numerical simulations

Pseudo-spectral calculations of the Boussinesq equations with rotation are performed on physically isotropic grids of  $\delta = 1$  and  $\delta = 0.25$  aspect-ratio domains with resolution ranging from  $512 \times 512 \times 128$  to  $2048 \times 2048 \times 512$ . We aim to explore how approach to the asymptotic limit  $\epsilon \rightarrow 0$  is different for  $\delta = 1$  and for  $\delta \ll 1$ . If we require isotropic resolution of the smallest resolved scales  $(k_x)_{\text{max}} = (k_y)_{\text{max}} = (k_z)_{\text{max}}$ , then  $N_x/N_z = L_x/L_z$ ,  $N_x = N_y$  and only modest  $\delta < 1$  is computationally feasible, even with rather large-scale computations by today's standards (e.g.,  $2048 \times 2048 \times 512$ , see Table 1). With an isotropic grid, it should be possible to adequately represent stratified turbulence for scales larger than the Ozmidov scale  $l_o = (\varepsilon_K/N^3)^{1/2}$ , as well as isotropic turbulence for scales smaller than  $l_o$ . The quantity  $\varepsilon_K$  is the flux of energy from large to small scales, and  $l_o$  gives an estimate for the length scale below which vertical overturning of waves is not prevented by the stratification. In order to approach the asymptotic regime in which potential vorticity is linear, it is necessary to consider  $N$  sufficiently large such that the Ozmidov scale and smaller scales are not resolved in our simulations. Nevertheless, an isotropic grid is a well-defined choice, which allows, with anticipated additional resources, the possibility of further grid refinement toward fully resolved flow for  $l < l_o$ .

The frequencies  $f$  and  $N$  are chosen such that the Burger number  $Bu = N\delta/f = 1$ . One simulation is also performed on a unit-aspect-ratio domain with resolution  $640^3$  in order to present a comparison with  $Bu = 1$  at unit aspect ratio. The computational domain has length  $L = 1$  on the horizontal and  $H = \delta$  in the vertical. Therefore the horizontal wavenumbers  $k_h$  are in integer multiples of  $\Delta k_h = 2\pi$  while the vertical wavenumbers  $k_z$  are in integer multiples of  $\Delta k_z = 2\pi/\delta$  yielding larger wavenumber increments in the vertical direction for  $\delta < 1$ . In all that follows, magnitudes in  $k_h$ ,  $k_z$  and  $k$  will be reported in units of  $2\pi$  for consistency, unless stated otherwise. Implicit in this choice is the understanding that the distribution of wavenumbers in the  $z$ -direction is sparser than in the horizontal for  $\delta < 1$  as described above. The time-stepping is implicit 4th-order Runge–Kutta with at least five timesteps per wave period of the fastest wave, that is  $\Delta t = 0.2\pi/(f + N)$ . The diffusion of both momentum and density (scalar) is modeled by hyperviscosity of Laplacian to the 8th power in order to extend the inertial scaling ranges. The Reynolds number in these cases is not computed explicitly but the hyperviscosity coefficient is dynamically chosen to resolve the total energy in the largest shell [43,12] at each timestep. Although



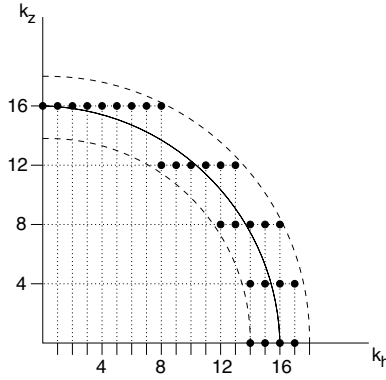


**Fig. 1.** Two-dimensional schematic of all wavevectors forced in shell  $3.5\Delta k_z \leq k < 4.5\Delta k_z$  where  $\Delta k_z = 2\pi/\delta = 4 \times 2\pi$ . The forced shell is bound by the dashed lines and all allowed wavevectors are marked by  $\bullet$ . The wavenumber values along the axes are marked in increments of  $2\pi$ . For each allowed value of  $k_z = \{4, 8, 12, 16\}$  note that there are multiple values of  $k_h$  that result in a wavevector within the shell.

this procedure and the use of up to power 8 in the Laplacian is very common in idealized studies such as this one, one caveat in using hyperviscosity is related to possible artifacts such as energy bottleneck and thermalization of the large wavenumbers [44]. We note that the flow features we observe are functions more of  $\delta$ ,  $f$  and  $N$  than of the hyperviscosity. Furthermore the hyperviscosity power is the same in all simulations thus presuming making any anomalous behavior common and hence not a factor in identifying differences between the flows. Certainly it is clear from simulations at unit aspect ratio that we have performed (not reported here) that using ‘normal’ Laplacian viscosity makes it quite difficult to discern the substantial spectral scaling ranges which we pursue in this study. While we are confident that hyperviscosity does not affect our primary conclusion, we nonetheless cannot completely rule out the possibility that it has some other more subtle or hidden consequences. The Prandtl number in all cases is  $\mathcal{O}(1)$ . The total energy input rate is fixed at  $\varepsilon_f = 1$  or  $\varepsilon_f = 0.5$  and  $Ro$  and  $Fr$  are varied by changing the rotation and stratification rates for fixed energy input rate which determines the nonlinear timescale. The simulations are dealiased according to the two-thirds dealiasing rule.

Our forcing is modeled after the stochastic scheme of [45] (see also [46] for use of this scheme in 3d isotropically forced Navier–Stokes turbulence) in which the wavenumbers  $k \leq 4.5\Delta k_z$  are stochastically forced. This ensures that the phase of each forced mode changes sufficiently rapidly so that the large scales will be statistically isotropic. At the beginning of each timestep, we choose a divergence-free forcing function,

$$\mathbf{f} = \nabla \times \Delta^{-1} \mathbf{g} \quad (16)$$

where the Fourier coefficients of  $\mathbf{g}$ , denoted by  $\tilde{\mathbf{g}}_{\mathbf{k}}$ , are chosen randomly with uniformly distributed phase and Gaussian distributed amplitude. Thus the forcing is incompressible, confined to the low wavenumbers (large scales) in a Gaussian distribution centered at  $k_f = 4\Delta k_z$  with shell width  $\Delta k_z$ . That is, for  $\delta = 0.25$ ,  $k_f = 16 \times 2\pi$  and for  $\delta = 1$ ,  $k_f = 4 \times 2\pi$ . The forcing magnitude is such that energy input is equipartitioned between the three velocity components and the density fluctuations. For  $\delta < 1$ , since the width of the forcing is a “thick” shell  $\Delta k_z$ , there is a bias in favor of horizontal wavenumber components. As an example, for  $k_z = 4 \times 2\pi/\delta$ , the shell with thickness  $3.5 \times 2\pi/\delta \leq k \leq 4.5 \times 2\pi/\delta$  has  $k_h < 16 \times 2\pi$ . A two-dimensional sketch of this example is given in Fig. 1. In that figure the black dots indicate all allowed wavevectors in the  $3.5 \times 2\pi/\delta \leq k \leq 4.5 \times 2\pi/\delta$  band. In order to check whether our results are biased in any way by such an apparently skewed forcing scheme, we have performed low

resolution  $256^3$  studies at unit aspect ratio with forcing distribution chosen to mimic Fig. 1. The resultant spectra were indistinguishable from those computed in simulations at the same resolution with the standard isotropically distributed forcing wavenumbers and other flow characteristics were qualitatively the same. Therefore we are somewhat assured that this forcing scheme does not bias our results in comparison to the case of isotropic forcing in a unit aspect-ratio domain.

Table 1 lists the parameters of the runs analyzed in this work. Note that, since our forcing inputs energy into all modes, we need to tune  $N$  and  $f$  to sufficiently high values (a maximum frequency of 10810 in runs 7 and 8) in order to achieve linear  $q$ . That is, since our effective forcing of nonlinear  $q$  does not automatically put our flow into a linear  $q$  regime we have to move to extremely large values of  $N$  and  $f$  which could result in under-resolved near-resonances. We believe that we have done the best possible analysis given current resources at these extreme values of  $N$  and  $f$  while being aware that calculations at even higher resolution, which we anticipate for future work, could indeed reveal differences. At our most extreme run at  $N = 10810$  we have performed a doubling of resolution from  $1024 \times 1024 \times 256$  to  $2048 \times 2048 \times 512$  to show that the spectra for the overlapping wavenumbers for those two simulations appear to have converged (see data analysis section below for details).

As mentioned in Section 2, the wave and vortical eigenmodes of the inviscid, linearized, unforced equations form a complete basis which can be used, without loss of generality, to represent the solution to the full nonlinear equations (see (4)–(5)). As will be shown, a significant difference between small- and unit-aspect-ratio  $Bu = 1$  flows is found for the energy spectrum associated with the wave component of the flow. The energy spectra of the wave and vortical components of the field are, respectively:

$$E^\pm(\mathbf{k}, t) = \frac{1}{2} \sum_{m=\pm} |b_m(\mathbf{k}, t)|^2 \quad (17)$$

$$E^0(\mathbf{k}, t) = \frac{1}{2} |b_0(\mathbf{k}, t)|^2. \quad (18)$$

For a more detailed analysis we can reconstruct, for example, the physical space wave and vortical contributions of the  $x$ -component of the velocity (which we will call the zonal component) as:

$$u_1^\pm(\mathbf{x}, t) = \text{ifft} \left( \sum_{m=\pm} b_m(\mathbf{k}, t) \phi_1^m(\mathbf{k}) \exp[i(\mathbf{k} \cdot \mathbf{x} - \sigma_m(\mathbf{k})t)] \right) \quad (19)$$

$$u_1^0(\mathbf{x}, t) = \text{ifft}(b_0(\mathbf{k}, t) \phi_1^0(\mathbf{k}) \exp[i(\mathbf{k} \cdot \mathbf{x} - \sigma_m(\mathbf{k})t)]) \quad (20)$$

where ifft is compact notation denoting the inverse Fourier transform over all  $\mathbf{k}$ . The horizontal kinetic energy spectrum of the flow can also be decomposed as:

$$E_h^\pm(\mathbf{k}, t) = \frac{1}{2} \sum_{i=1,2} \sum_{m=\pm} |b_m(\mathbf{k}, t) \phi_i^m(\mathbf{k})|^2 \quad (21)$$

$$E_h^0(\mathbf{k}, t) = \frac{1}{2} \sum_{i=1,2} |b_0(\mathbf{k}, t) \phi_i^0(\mathbf{k})|^2. \quad (22)$$

With  $\phi_i^m = \tilde{u}_i^m$  for  $i = 1, 2, 3$  and  $\phi_i^m = \tilde{\rho}^m$  for  $i = 4$ , the vertical velocity and the scalar can thus be analogously decomposed. The definitions (17)–(22) will be used in Section 4 in our analysis of the physical and spectral space field for the horizontal velocity.

All runs and visualizations were performed using the computational resources at Argonne Leadership Computing Facility (ALCF, Argonne National Laboratory) on the Blue Gene/P (Intrepid) machine. The most computationally intensive run 6 used about 15 million CPU hours. All the runs together required approximately 25 million CPU hours.

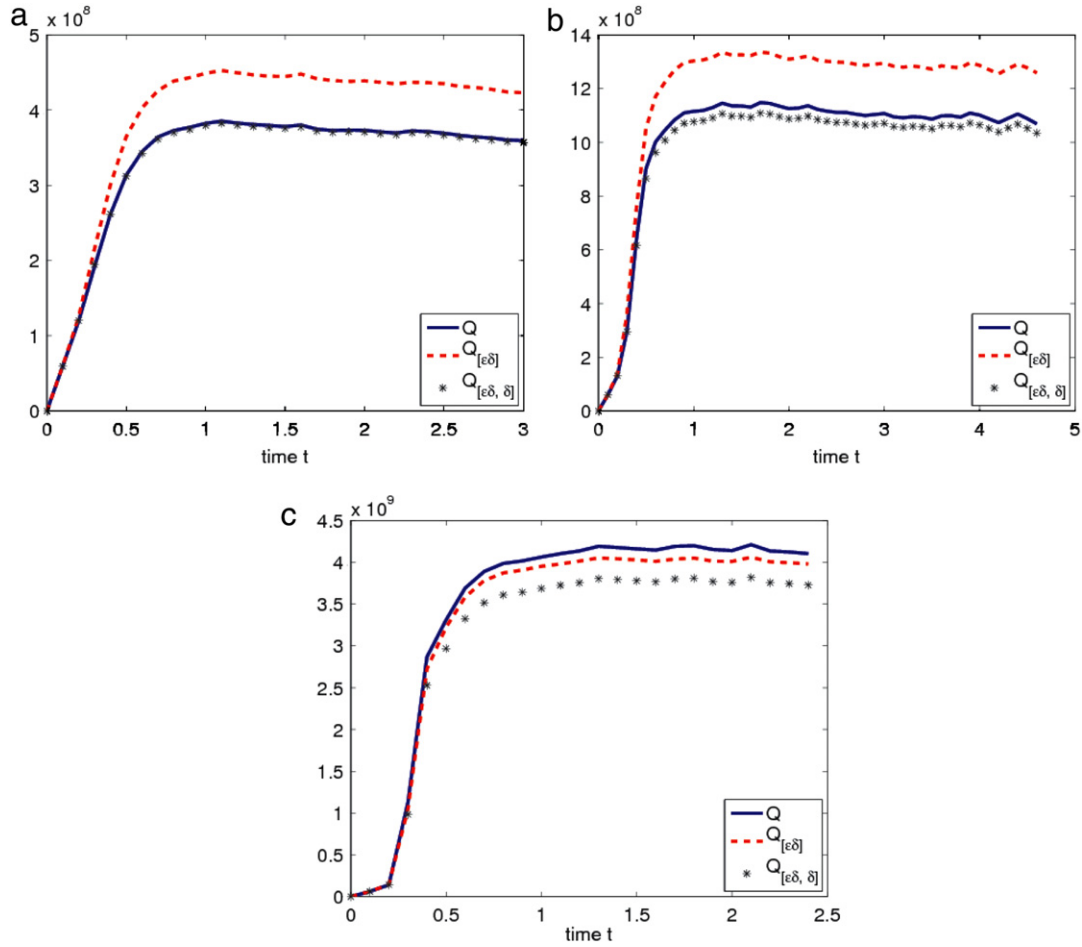


**Fig. 2.** Study of increasing grid resolution for  $\delta = 0.25$  and moderately small  $\epsilon = 0.05$ . Evolution in time of total potential enstrophy  $Q$ , and contributions  $Q_{[\epsilon\delta, \delta]}$  and  $Q_{[\epsilon\delta]}$  for (a) run 1, grid  $512 \times 512 \times 128$  (b) run 2, grid  $1024 \times 1024 \times 256$  and (c) run 3, grid  $2048 \times 2048 \times 512$ . In all cases the desired asymptotic regime of  $Q \simeq Q_{[\epsilon\delta, \delta]} \simeq Q_{[\epsilon\delta]}$  has clearly not been achieved, suggesting that  $\epsilon$  is not small enough.

## 4. Data analysis

### 4.1. Increasing grid resolution for $\epsilon = 0.05$ and $\delta = 0.25$

We first study the effect of increasing resolution (with corresponding increase in Reynolds number based on the ratio of nonlinear to hyperviscous terms) for fixed  $\delta = 0.25$  and moderate  $\epsilon = 0.05$ . Runs 1, 2 and 3 are a series of simulations for isotropic grid and grids  $512 \times 512 \times 128$ ,  $1024 \times 1024 \times 256$  to  $2048 \times 2048 \times 512$ , doubling resolution with each increasing in number of grid points. Since the hyperviscosity coefficient scales according to the scheme of [43] (see above) our Reynolds number is effectively increasing in this series of runs. Fig. 2 shows the evolution of potential enstrophy in time as resolution increases (panels (a)–(c)). While the potential enstrophy saturates in time for all three cases, it is clear that the asymptotic regime of  $Q \simeq Q_{[\epsilon\delta, \delta]} \simeq Q_{[\epsilon\delta]}$  corresponding to linear  $q$  has not been achieved for  $\epsilon = 0.05$ . Fig. 3 shows the wave (Eq. (17)), vortical (Eq. (18)) and total energy spectra (panels (a)–(c)) as the resolution increases. We see that the wave spectra have not converged at any of the scales with scaling ranging from  $k^{-4/3}$  at the lowest resolution and  $k^{-5/3}$  at the highest resolution. The vortical spectra have converged in the range over which the wavenumbers of the three resolutions overlap with scaling in that range slightly shallower than  $k^{-3}$ . The extended range for the vortical spectra show a significant shallowing for runs 2 and 3. These observations indicate that the neither the wave nor the vortical mode energies have achieved the asymptotic behavior

expected for  $\epsilon \rightarrow 0$ . Panel (d) of Fig. 3 puts the wave, vortical and total energies together for the highest resolution run 3 showing the clear dual range scaling of the vortical energy from slightly shallower than  $k^{-3}$  to much shallower, and the nearly  $k^{-5/3}$  scaling of the wave energy. For fixed, moderately small  $\epsilon = 0.05$ , this study in increasing resolution shows that the small scales of the flow are still affected by nonlinear potential vorticity.

### 4.2. Decreasing $Ro = Fr = \epsilon$ for fixed $\delta = 0.25$ and fixed resolution

We next study the effect of tuning  $\epsilon$  down to smaller values for fixed aspect ratio  $\delta = 0.25$ , fixing the resolution at the highest available,  $2048 \times 2048 \times 512$ . The aim is to discover what happens in the intermediate and asymptotic regimes as linear  $q$  (quadratic potential enstrophy  $Q$ ) is achieved. Fig. 4 shows the evolution in time of potential enstrophy as  $\epsilon$  decreases from 0.05 down to 0.002 (panels (a)–(d), runs 3, 4, 5 and 6). As  $\epsilon$  decreases by a factor 5 from 0.05 to 0.01 (runs 3 and 4 in panels (a) and (b)) we see that  $Q \simeq Q_{[\epsilon\delta, \delta]}$  indicated by the coincidence of the solid line and the  $\times$ 's. This indicates that the flow has achieved an intermediate state wherein contributions to  $q$  from the  $\mathcal{O}(\delta)$  terms are still significant. As  $\epsilon$  is reduced to 0.005 (panel (c)) the  $Q \simeq Q_{[\epsilon\delta, \delta]}$  behavior persists but the asymptotic regime of  $Q \simeq Q_{[\epsilon\delta, \delta]} \simeq Q_{[\epsilon\delta]}$  has still not been achieved as shown by the peeling away of the dashed line from the solid line and  $\times$ 's. Note also that the potential enstrophy in run 5 has not achieved steady state. However, given that the trend away from the asymptotic state of linear  $q$  seemed clear, we terminated run 5 in the interest of pursuing an even lower  $\epsilon$  case.

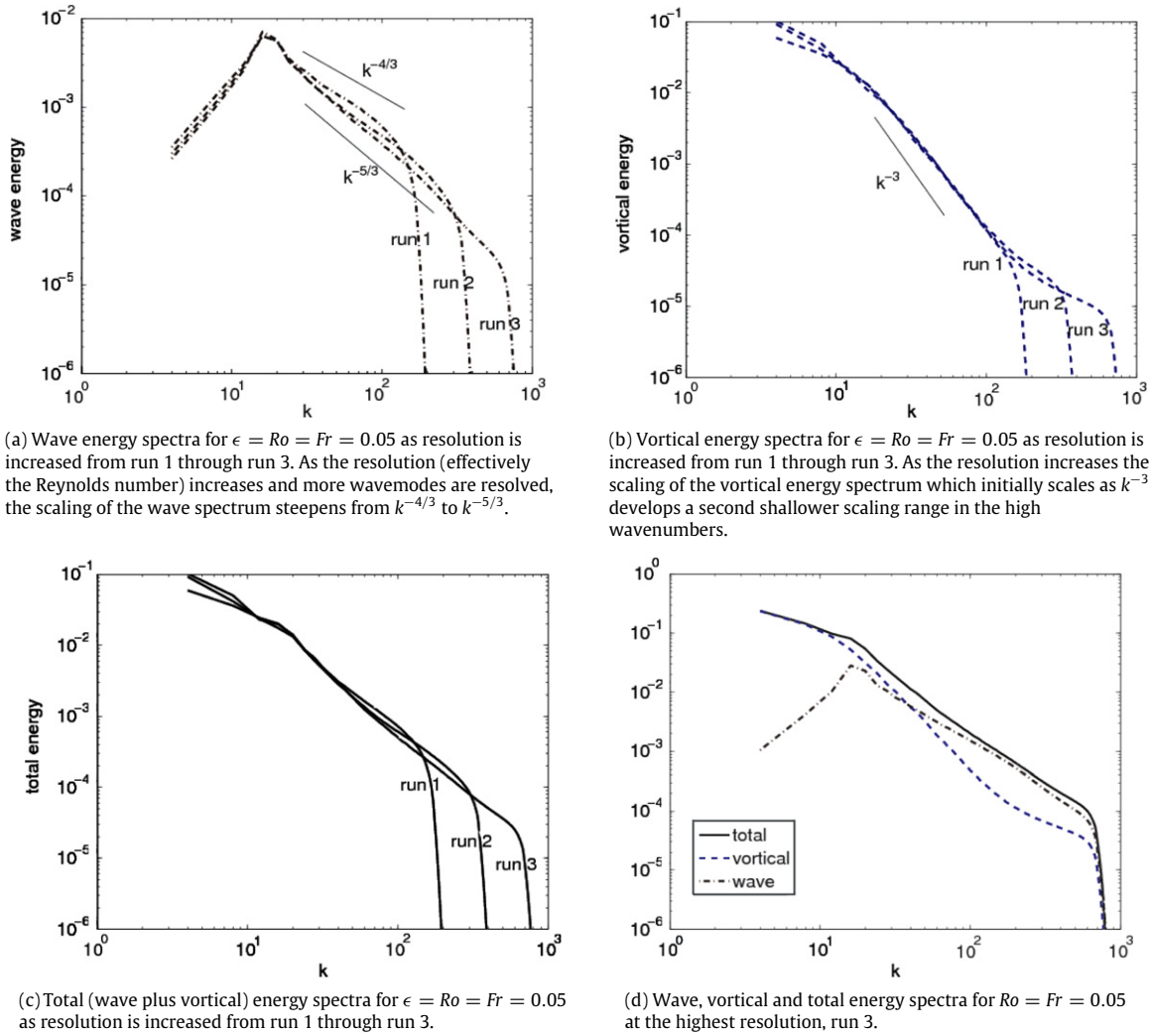


**Fig. 3.** For  $Ro = Fr = 0.05$  and  $\delta = 0.25$ , a comparison of wave, vortical and total (wave plus vortical) energy spectra for (a) run 1, (b) run 2 and (c) run 3 at latest times  $t = 3, 4.6$  and  $2.4$  respectively, showing the trend as resolution (effectively the Reynolds number) is increased. In all cases, the modes  $k > k_f$  have achieved (nearly) statistically steady state. Panel (d) shows the wave, vortical and total spectra for the highest resolution run 3.

At the lowest values of  $\epsilon = 0.002$  (run 6, panel (d)) we see clearly that  $Q \simeq Q_{[\epsilon\delta, \delta]} \simeq Q_{[\epsilon\delta]}$  thus indicating that potential enstrophy has achieved its asymptotic quadratic value. It is this case that we will explore further as the cornerstone in our study of  $Bu = 1$  for small aspect ratio and asymptotically small  $\epsilon$ .

The evolution of the wave, vortical and total energies in time corresponding to the study in decreasing  $\epsilon$  are given in Fig. 5. Progressing from panels (a) through (d) we note that the wave energy, expected to dominate the small scales, has saturated for the two larger values of  $\epsilon$  ((a) and (b)) but is still growing, albeit quite slowly for the two small  $\epsilon$  ((c) and (d)). Thus, for the smallest  $\epsilon$  cases, by one measure of the small scales, namely the potential enstrophy, the small scales have saturated (see Fig. 4(d)). However, by the measure of wave energy, the small scales (high wavenumbers) have not achieved strictly statistically steady state. The vortical energy in all cases is expected to grow in the low wavenumbers, and since we do not have a sink for the energy in the low wavenumbers we do not expect the vortical energy to saturate, consistent with observations.

The spectra of the wave, vortical and total energies for decreasing  $\epsilon$  are given in Fig. 6. In each case we plot the spectra at the latest time for a particular run since for the two lowest  $\epsilon$  the wave spectra for  $k > k_f$  are not statistically steady but are still slowly growing. Thus we would not be justified in presenting time-averaged spectra in these cases. Progressing from (a) to

(d) for decreasing  $\epsilon$  in Fig. 6, we note that the vortical energy transitions smoothly from a dual scaling of nearly  $k^{-3}$  followed by a much shallower range (panel (a)), to a  $k^{-3}$  scaling over the entire  $k > k_f$  range (panel (d)). This is the classical QG scaling of the vortical modes expected as  $q$  becomes asymptotically linear and is identical to what one observes for small  $\epsilon$  at  $\delta = 1$  (see discussion below). However, as  $\epsilon$  is decreased, the wave energy spectra settle on a final distribution quite different from what is known for the  $\delta = 1$  case. From the largest  $\epsilon = 0.05$  case in panel (a) where the wave spectrum scales approximately as  $k^{-5/3}$ , it transitions through a regime where it scales nearly as  $k^{-2}$  followed by a range of pile-up of energy with no distinguishable ‘scaling’. And finally at  $\epsilon = 0.002$  it settles to a  $k^{-2.5}$  scaling followed by a shallower range of approximately  $k^{-4/3}$ . In all the scalings discussed, note that the lines shown in the graphs are to be used as a guide to the eye rather than as strict measurements. We do not provide exact measurements of scaling exponents in these previously unexplored regimes, apart from the known  $k^{-3}$  for 3DQG, as we do not have any expectations or comparisons to validate.

As we have noted above, the case for smallest  $\epsilon$  at the highest resolution (run 6) achieved steady state for total potential enstrophy, but not for the wave energy in time. This is reflected in our observation that the wave energy spectrum for this run is still very slowly growing in time in the high wavenumbers. This could be a result of not having run long enough, however,

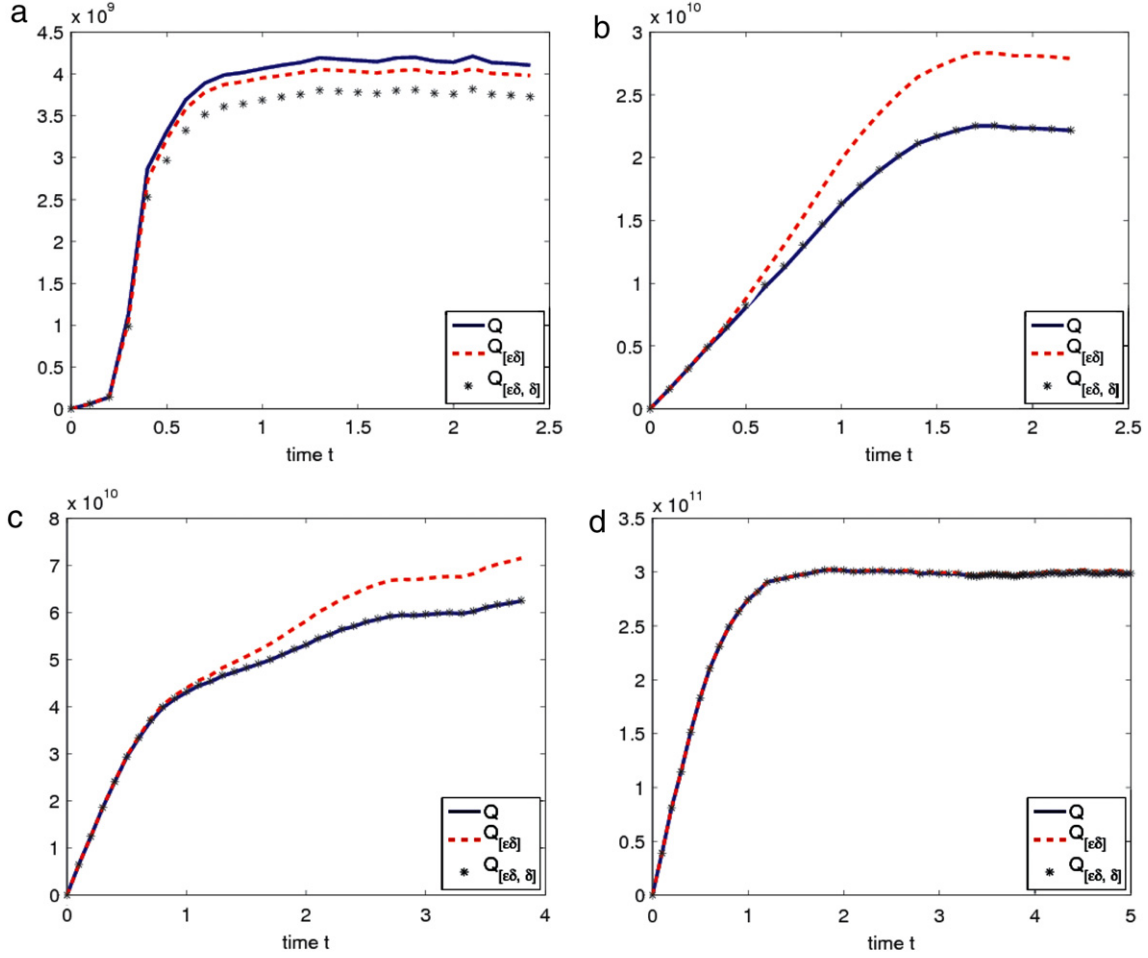


**Fig. 4.** Study of decreasing  $\epsilon$  for fixed  $\delta = 0.25$  and fixed resolution  $2048 \times 2048 \times 512$ . Evolution in time of total potential enstrophy  $Q$ , and contributions  $Q_{[\epsilon\delta]}$  and  $Q_{[\epsilon\delta, \delta]}$  for (a) run 3,  $\epsilon = 0.05$ , (b) run 4,  $\epsilon = 0.01$ , (c) run 5,  $\epsilon = 0.005$  and (d) run 6,  $\epsilon = 0.002$ . As  $\epsilon$  decreases,  $Q \simeq Q_{[\epsilon\delta, \delta]}$  (panels (b, c, d)). The asymptotic regime of  $Q \simeq Q_{[\epsilon\delta, \delta]} \simeq Q_{[\epsilon\delta]}$  is only observed in panel (d) for the lowest value of  $\epsilon = Ro = Fr = 0.002$ , where the solid line,  $\times$ 's and dashed line lie indistinguishably on top of each other.

running longer could introduce contamination by the developing large scales. It is also possible that we are still under-resolved at  $2048 \times 2048 \times 512$  and thus not adequately resolving wave-interactions at these extreme values of  $N$  and  $f$ . Thus we ran an extra case (run 7) at half the grid resolution of run 6 keeping  $N$  and  $f$  fixed. The wave, vortical and total spectra of both runs 6 and 7 are plotted together at  $t = 4.2$  in Fig. 7. For  $k < 300$  which is approximately  $k_{\max}$  for run 7, the wave spectrum indeed shows a scaling of near  $k^{-2.5}$  and appears to have converged. While this does not rule out under-resolution effects for  $k > 300$  in run 6, it fairly definitively establishes a wave spectral scaling much steeper than the  $k^{-1}$  observed at unit aspect ratio. Our main point is that the wavemodes for  $\delta < 1$  behave differently than the wavemodes for  $\delta = 1$  in the asymptotically small  $\epsilon$  regime; we believe that this has been established to the extent possible with our significant use of computational resources.

For completeness, we present the potential enstrophy and spectra for the case  $\delta = 1$ , run 8. These results have already been reported in [14,15] and similar results are familiar from many studies of this regimes, but are repeated here for convenience. In unit aspect ratio, the leading order contribution to  $q$  in the linear regime is  $\mathcal{O}(\epsilon\delta) = \mathcal{O}(\epsilon)$ . Correspondingly, Fig. 8(a) shows that indeed we are in the nearly quadratic  $Q$  (linear  $q$ ) in our unit-aspect-ratio run and that the global potential enstrophy has reached statistically state. Fig. 8(b) shows that the wave component of the energy has also saturated while the vortical

component has not. The latter is expected given that there is no sink for the energy in the large scales. Fig. 8(c) shows the familiar  $k^{-1}$  scaling of the wave energy spectrum, and the  $k^{-3}$  scaling of the vortical energy spectrum in the flow. When compared with the run 6 for  $\delta = 0.25$  it is clear that the difference between the  $Bu = 1$  flows lies in the wave component while the similarity lies in the 3DQG scaling of the vortical component.

#### 4.3. Physical and spectral space analysis of horizontal velocity

In further investigation, we compare the properties of the horizontal flow velocity of the  $\delta = 0.25$  case as compared to the  $\delta = 1$  case at  $\epsilon \simeq 0.002$ . Specifically we will look at the eigenmode decomposition of the horizontal velocity, separating the wave and vortical components, and compare the physical space visual flow characteristics, spectra of the wave component and certain phenomenological aspects. We project the wave component of the zonal velocity in physical space according to Eq. (20) at the latest times for runs 6 and 8. A similar procedure is performed for the vortical field. In Fig. 9 we show a comparison between runs 6 and 8 for the total, vortical and wave projections of the zonal velocity field. The visualizations are of surface contours with the starkest difference appearing between the wave components (panels (e) and (f)) of the two flows. The  $\delta = 0.25$  flow shows a distinct layered structure over the vertical width of which the sign of the velocity changes (red to blue). This layered structure is different



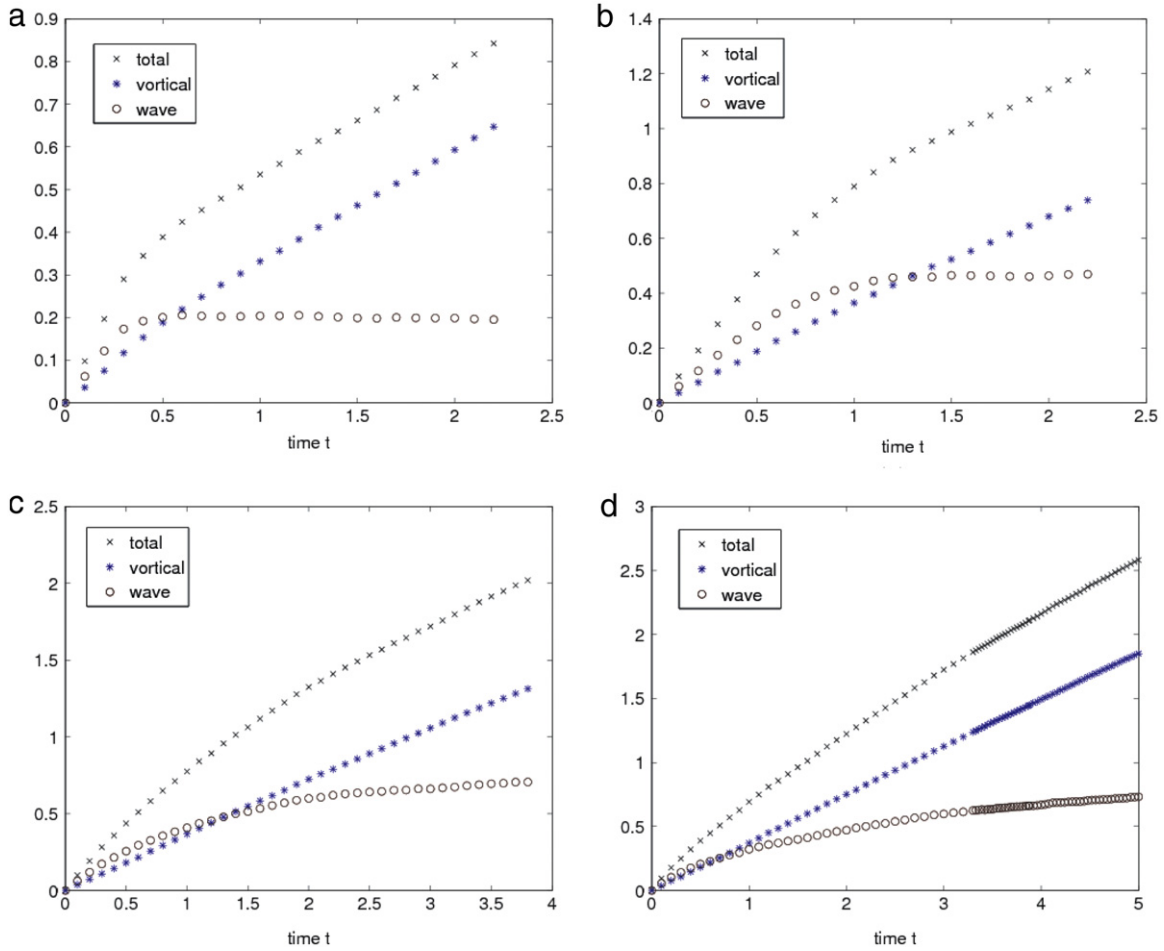


**Fig. 5.** Study of decreasing  $\epsilon$  for fixed  $\delta = 0.25$  and fixed grid resolution  $2048 \times 2048 \times 512$ . Evolution in time of wave, vortical and total energies for (a) run 3,  $\epsilon = 0.05$ , (b) run 4,  $\epsilon = 0.01$ , and (c) run 5,  $\epsilon = 0.005$ , (d) run 6,  $\epsilon = 0.002$ .

from the VSHF associated with  $Bu \gg 1$  flows because the layers do not extend the entire width of the box and the flow does not have a strong  $k_h = 0$  component (see Fig. 7). We also zoom in on a  $512 \times 512 \times 512$  subset of run 6 at latest time and show the zonal velocity surface contours in Fig. 10, again for total, wave and vortical projections. The layered structure of the wave component is again apparent.

Given the distinct appearances of the wave component of the horizontal flow in visualizations of the two  $Bu = 1$  flows for small  $\epsilon$ , we next compare the spectral distribution in wavenumber of the horizontal wave energy. We plot the horizontal wave energy of run 6 ( $\delta = 0.25$ ) both as a function of  $k_h$  (summed over  $k_z$ ) and as a function of  $k_z$  (summed over  $k_h$ ). The result is shown in Fig. 11(a) with a similar plot for run 8 ( $\delta = 1$ ) in Fig. 11(b) for comparison. In both runs the wave energy as a function of  $k_h$  saturates for  $k_h < k_f$  (dashed lines) while the behavior in  $k_z$  drops off sharply as  $k_z < k_f$  (solid lines). The similarities end there. The small-scale behavior is completely different for the two flows. For the  $\delta = 0.25$  flow the horizontal wave energy spectrum decays as  $k_h^{-2}$  while for  $\delta = 1$  the spectrum decays as  $k_h^{-1}$ . In both cases the wave energy spectrum as a function of  $k_z$  (solid line) contains the majority of the downscale (high wavenumber) energy. Again the similarities end there because the distribution of energy in  $k_z$  in (a) shows a dual scaling regime of  $k_z^{-2}$  followed by a regime with much shallower scaling, almost a ‘pile-up’, whereas in (b) there scaling is approximately  $k_z^{-1}$  albeit with a slightly longer scaling regime than in  $k_h$ , with no evidence of a second scaling range.

#### 4.3.1. A phenomenology for spectral scaling of horizontal kinetic energy

In this section we describe a phenomenological model for the horizontal kinetic energy spectra in the asymptotic limit of  $\epsilon \rightarrow 0$  for  $\delta < 1$ . The model was first proposed for  $\delta = 1$  in [14] for  $Bu = 1$ , and extended to  $Bu \ll 1$  and  $Bu \gg 1$  [15]. We will here sketch how it can be extended consistently to the  $\delta < 1$  case. For flow in the linear potential vorticity regime, dimensionally, the potential vorticity is,

$$\text{in physical space } q = f \partial_z \rho - N \boldsymbol{\omega} \cdot \hat{\mathbf{z}} \quad (23)$$

$$\text{and in Fourier } \tilde{q} = -i(fk_z \tilde{\rho} - Nk_h \times \tilde{u}_h) \simeq -i(fk_z \tilde{\rho} - Nk_h \tilde{u}_h) \quad (24)$$

where the last  $\simeq$  is allowed by the empirically observed smallness of the vertical velocity in such flows for large  $N$ . We define the parameter

$$\Gamma(\mathbf{k}) = \frac{fk_z}{Nk_h} \quad (25)$$

where  $k_h$  and  $k_z$  are the horizontal and vertical components of the wavevector respectively. The parameter  $\Gamma$  picks out the relative importance of rotation to stratification in the potential vorticity with respect to scale. The value  $\Gamma = 1$  is defined by the surface of a cone in spectral space with angle  $\phi$  to the vertical given by  $\tan(\phi) = k_h/k_z = f/N$ . For fixed  $f$  and  $N$ , wavevectors  $\mathbf{k}$  giving  $\Gamma \ll 1$  lie outside the cone, while those giving  $\Gamma \gg 1$  lie inside

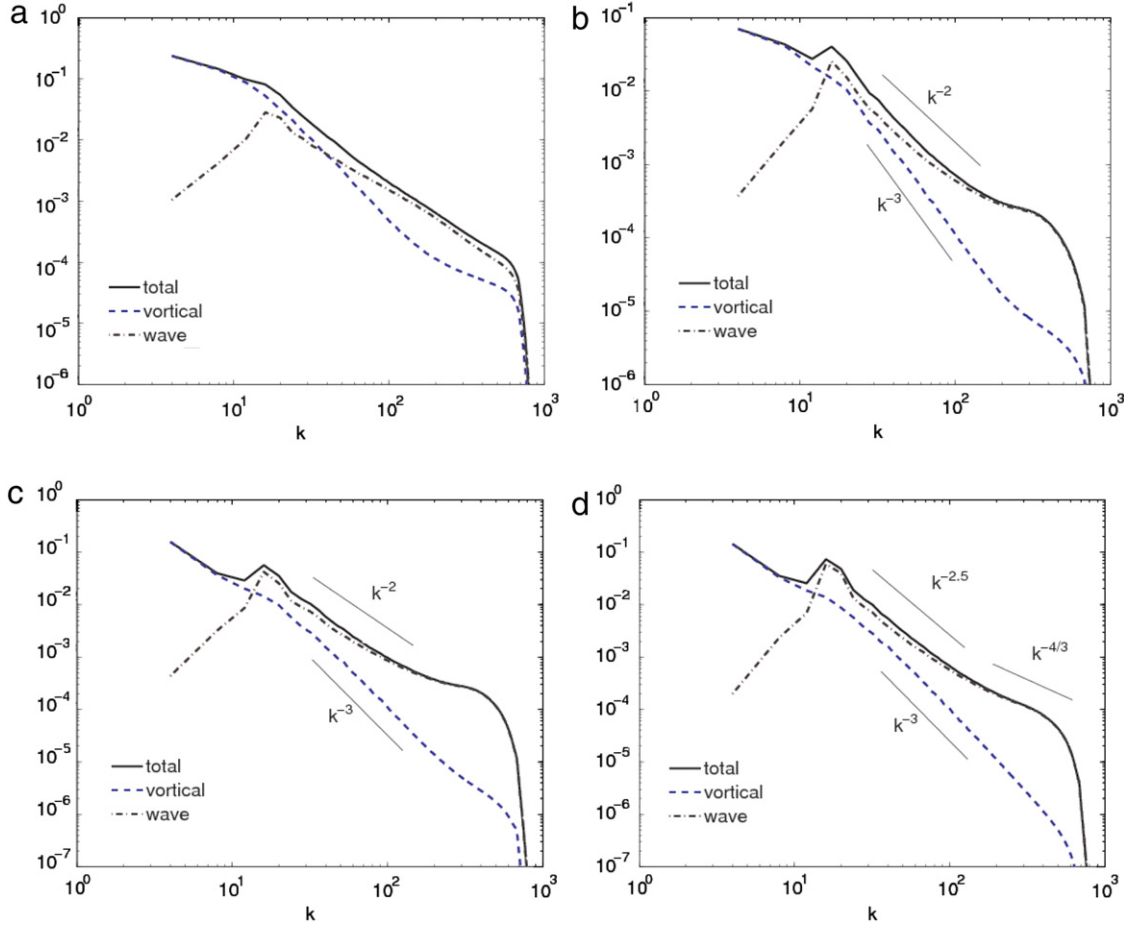


**Fig. 6.** Wave, vortical and total energy spectra for fixed  $\delta = 0.25$ , fixed grid  $2048 \times 2048 \times 512$  and (a) run 3,  $\epsilon = 0.05$  (b) run 4,  $\epsilon = 0.01$ , (c) run 5,  $\epsilon = 0.005$  and (d) run 6,  $\epsilon = 0.002$ . In each case the spectra are plotted at the latest time of the run, after both the total potential enstrophy and the wave energy in modes  $k > k_f$  have achieved (nearly) statistically steady state. As  $\epsilon$  is decreased the vortical mode energy recovers  $k^{-3}$  scaling of 3DQG throughout the range  $k > k_f$ , while the wave mode energy spectrum steepens through a range of transient behaviors finally settling on a scaling of about  $k^{-2.5}$  followed by a second, much shallower range. The scaling lines indicated are given as guides to the eye.

the cone (see Fig. 12). The extreme case of stratification dominated flows  $f/N \ll 1$  for a finite box such that  $f/N \ll k_h/k_z$  for a wide range of  $k$ , gives a very narrow critical cone with wavenumbers lying mostly outside the cone ( $\Gamma \ll 1$ ) and scaling in  $k$  becomes independent of  $k_z$ . The opposite extreme case of rotating dominated flows  $f/N \gg 1$  gives a very wide critical cone with wavenumbers lying mostly inside the cone ( $\Gamma \gg 1$ ) and the scaling in  $k$  becomes independent of  $k_h$  for a finite box size.

The  $Bu = 1$  cases we consider do not fall in the extreme  $f/N$  regimes and therefore are expected to exhibit some intermediate behavior in  $k_h$  and  $k_z$ . In our run 6, for  $Bu = 1$  and  $\delta = 0.25$  we have  $f/N = 0.25$ . For this flow  $\Gamma = 1$  is a cone of angle  $\phi = \arctan(f/N) = 14^\circ = 1/4$  rad. In our unit-aspect-ratio run 8,  $Bu = 1$  and  $\delta = 1$  we have  $f/N = 1$ , and  $\Gamma = 1$  is a cone of angle  $\phi = \arctan(f/N) = 45^\circ = \pi/4$  rad. The two critical cones are shown in Fig. 12. It is immediately apparent that for the  $\delta = 1$  case on the left, the wavenumbers are distributed evenly on both sides of the critical cone and we thus expect that neither stratification nor rotation will dominate. This is consistent with the visualizations of the flow which do not exhibit either columnar or layered structures. For the  $\delta = 0.25$  case on the right of Fig. 12, a small majority of wavenumbers will fall in the  $\Gamma \ll 1$  sector thus giving a slight preference for the stratification part of linear  $q$ . In this sense one can see that stratification effects might be somewhat dominant in aspects of the flow at  $Bu = 1$  for small aspect ratio.

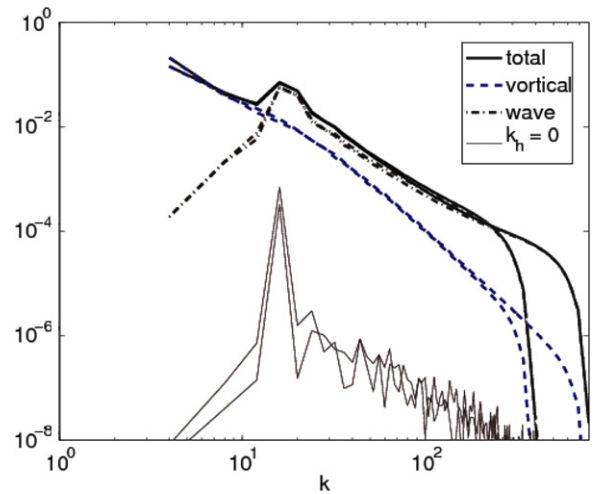


**Fig. 7.** Runs 6 and 7, doubling resolution for  $\epsilon = 0.002$ . Spectra are plotted at the same time  $t = 4.2$  and show reasonable convergence for  $k < 300$ , the maximum  $k$  for the lower resolution case. This plot also shows that the energy of the  $k_h = 0$  wave modes are the negligible contribution to the total energy.

We here briefly review the relevant parts of the phenomenological discussion for  $\Gamma \ll 1$ , the details of which may be found in

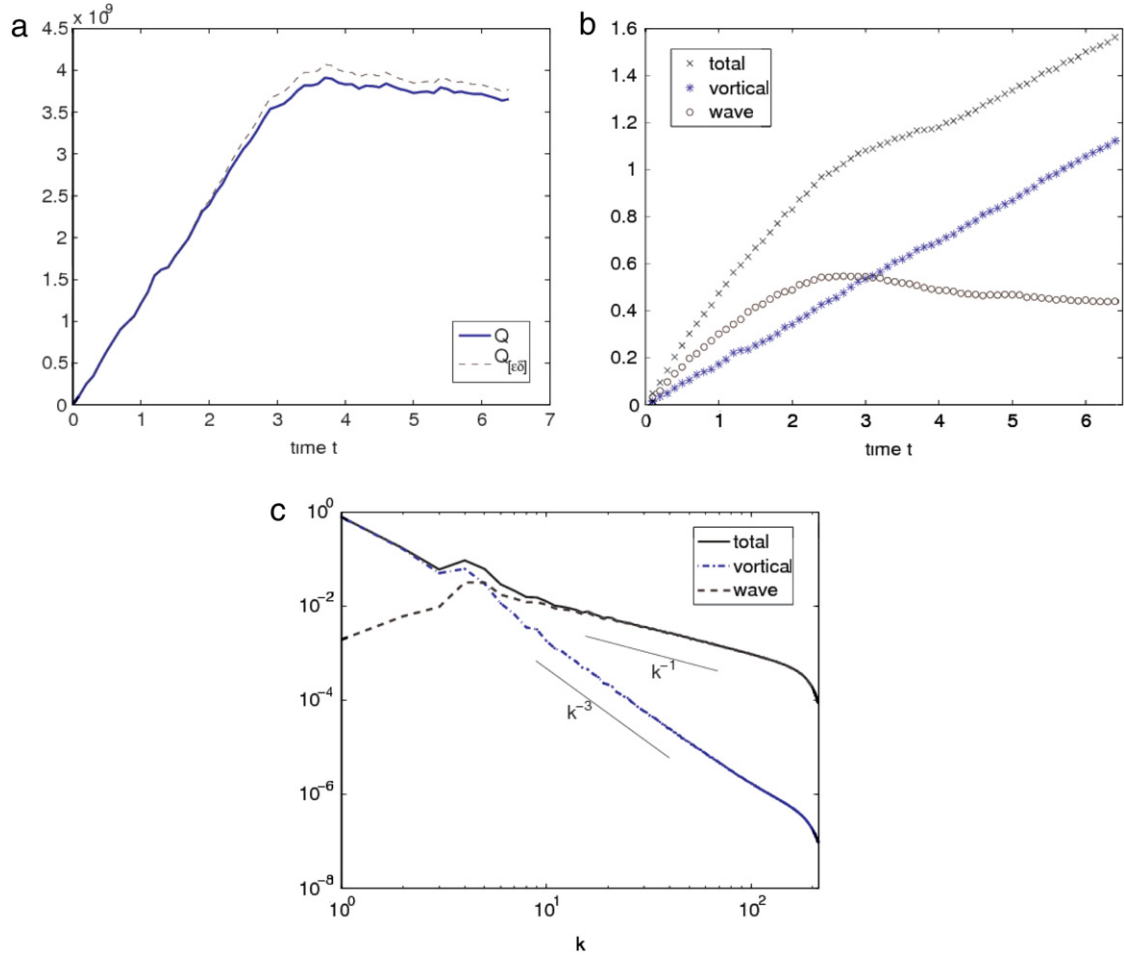


**Fig. 8.** For run 8 at unit aspect ratio  $\delta = 1$ , and  $Ro = Fr = 0.0023$ , (a) potential enstrophy evolution showing that  $Q \simeq Q_{[\epsilon\delta]}$ ; (b) evolution in time of the wave, vortical and total energies and (c) wave, vortical and total energy spectra. The vortical energy achieves 3DQG scaling of  $k^{-3}$  while the wave energy scales as  $k^{-1}$ . The spectra are plotted at the latest time of the run after the total potential enstrophy and the wave energy in modes  $k > k_f$  have achieved statistically steady state.

[14,15]. When the stratification component of linear  $q$  dominates in a Fourier mode  $k$ , one can write:

$$\text{stratification dominates } q \quad \tilde{q}(k) \simeq iNk_h \tilde{u}_h, \quad (26)$$

$$\text{and } Q(k) \simeq \frac{1}{2} |Nk_h \tilde{u}_h|^2, \quad (27)$$

$$\text{with constraint } \lim_{\kappa_h \rightarrow \infty} \int_{\kappa_h}^{\infty} Q(k) dk_h \gg N^2 \kappa_h^2 \int_{\kappa_h}^{\infty} E_h(k) dk_h. \quad (28)$$

Eq. (28) is interpreted to mean that for wavevectors with large  $k_h$ , that is the ‘wide’ wavevectors, the potential enstrophy  $Q(k)$  dominates the downscale (horizontal scales smaller than  $1/\kappa_h$ ) dynamics and consequently suppresses the transfer of horizontal kinetic energy into those modes. This is analogous to the relation in 2d turbulence

$$\lim_{\kappa \rightarrow \infty} \int_{\kappa}^{\infty} \Omega(k) dk \gg \kappa^2 \int_{\kappa}^{\infty} E(k) dk \quad (29)$$

wherein the enstrophy  $\Omega(k)$  suppresses the downscale transfer of kinetic energy  $E(k)$  for sufficiently high wavenumber  $\kappa$ , and in turn forces the inverse cascade of energy. More generally, for fixed  $f/N$  there is a transition regime when  $k_h/k_z \simeq f/N$ . Thus, in an idealized infinite wavenumber flow, for fixed  $f/N$  there will be some regime of wavevectors such that  $k_h/k_z \gg f/N$  for which  $\Gamma \ll 1$  and horizontal kinetic energy is suppressed along  $k_h$ . The range in  $k$ -space over which  $\Gamma \ll 1$  depends on where the critical

cone  $\Gamma = 1$  lies and the difference for the two  $Bu = 1$  cases is apparent from Fig. 12.

For  $\Gamma \ll 1$  the potential enstrophy suppresses transfer of horizontal kinetic energy to the large  $k_h$  for small  $k_z$  resulting in a prediction for steep drop-off in energy in  $k_h$ . In [14,15] we measured empirically the scaling to be  $E_h(k_h, k_z) \sim k_h^{-5}$  for small  $k_z$ . In Fig. 13(a) we plot  $E_h(k_h, k_z)$  as a function of  $k_h$  for various fixed  $k_z$ . Observe that for  $k_z/k_h < N/f = 4$ , the horizontal kinetic energy spectrum steepens to very close to  $k_h^{-5}$ . However, since the range of steep scaling depends on  $k_z$ , the net effect on  $E_h(k_h, k_z)$ , when summed over  $k_z$ , gives a shallower  $k_h^{-2.5}$  scaling of  $E_h(k_h)$  (Fig. 13(b)).

In Fig. 14 the horizontal kinetic energy is plotted for  $\delta = 1$ , run 8, showing qualitatively very similar behavior as for the  $\delta = 0.25$  case (Fig. 13), except that, because the scaling transition to steep  $k_h^{-5}$  behavior happens as  $k_z/k_h < N/f = 1$ , the shape of the spectrum when summed over  $k_z$  is different from the  $\delta = 0.25$  case, even though  $Bu = 1$  in both cases. The greater area associated with  $\Gamma \ll 1$  for  $Bu = 1$ ,  $\delta = 0.25$  in Fig. 12 (the stratification dominated potential vorticity regime), is consistent with the observed evidence of layered structure in Fig. 9(e).

## 5. Conclusions

We have performed high resolution, computationally intensive simulations of the Boussinesq equations with rotation, characterized by isotropic grids in physical space and at least five timesteps

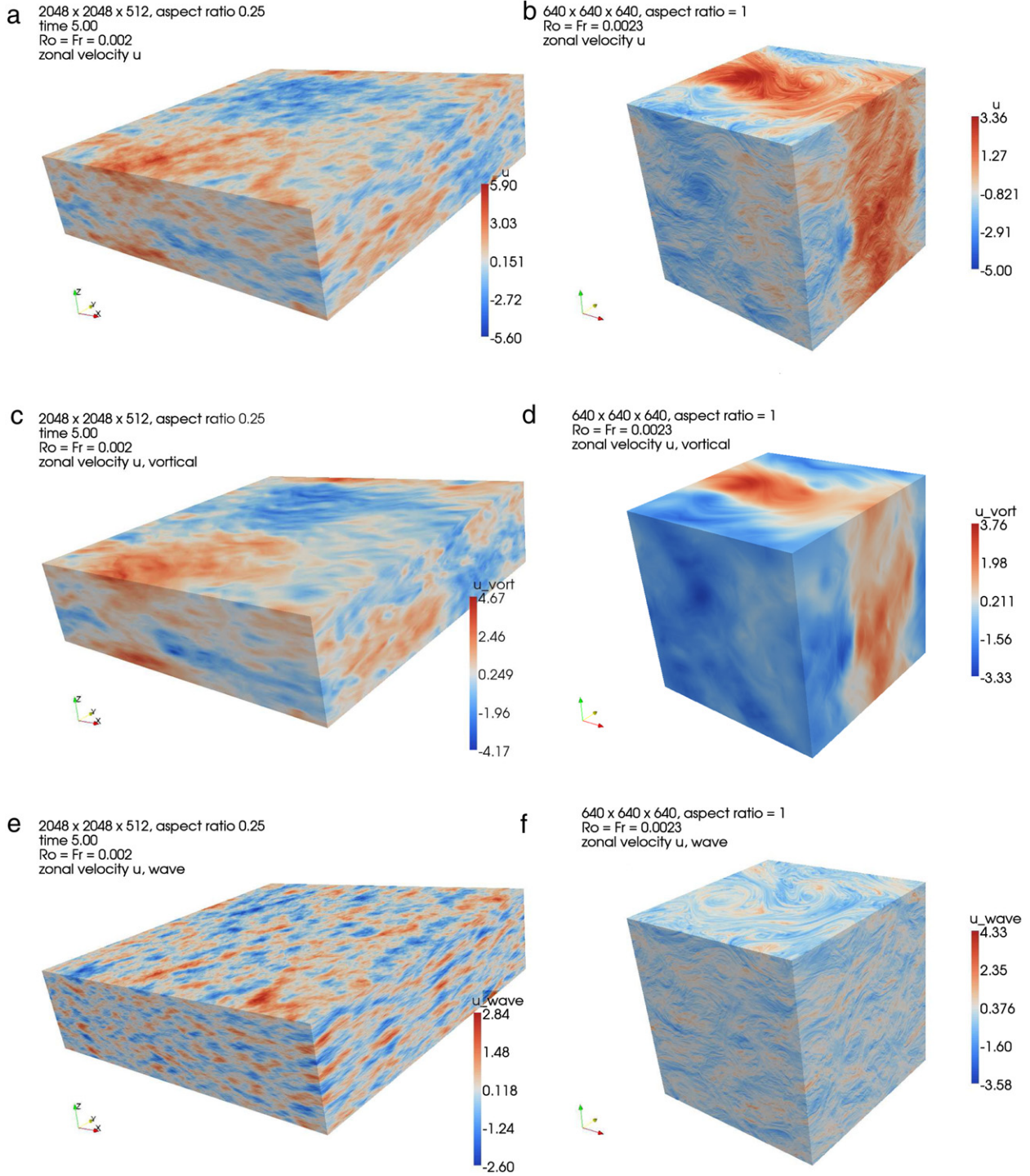


**Fig. 9.** (Color online) Visualization comparing surface contours of the  $x$ -component of the velocity for  $\delta = 0.25$ ,  $\epsilon = 0.002$ , run 6 (a, c, e) and  $\delta = 1$ ,  $\epsilon = 0.0023$ , run 8 (b, d, f). For each  $\delta$  the total (top row), vortical (middle row) and wave (bottom row) components of the flow are visualized. Red indicates flow along positive  $x$ -direction and blue its reverse. The comparison of wave mode velocity in particular (panels (e) and (f)) illustrates the qualitative difference between small-aspect-ratio flow which has a layered structure, and unit-aspect-ratio flow which has no layered structure, for almost equal  $\epsilon$  and  $Bu = 1$ .

per period of the fastest wave frequencies. Our study initiates a quantitative comparison of the small scales of  $Bu = 1$  flows with small aspect ratio  $\delta \ll 1$  and unit aspect ratio  $\delta = 1$ , for low wavenumber (large-scale) forcing, and with  $f$  and  $N$  tuned to values such that potential enstrophy approached regimes consistent with linear potential vorticity. For  $\delta = 1/4$  and  $\delta = 1$ , we have shown that the two flows are similar in some respects and very different in others. The energy of the vortical mode in small scales is qualitatively (visually) and quantitatively (in terms of scaling of

the spectra) the same. The difference between the two flows arises in the wave component which exhibits a layered structure for the  $\delta = 0.25$  case and scaling steeper than  $k^{-1}$  in the wave energy spectrum. Since  $k^{-1}$  has been expected and observed in numerous studies for the wave energy at  $\delta = 1$ , we conclude that the  $\epsilon \rightarrow 0$  asymptotics in  $Bu = 1$  flows are perhaps non-universal and depend on the aspect ratio even for asymptotically small  $\epsilon$ . We hope that this work motivates more rigorous theoretical understanding of these issues.



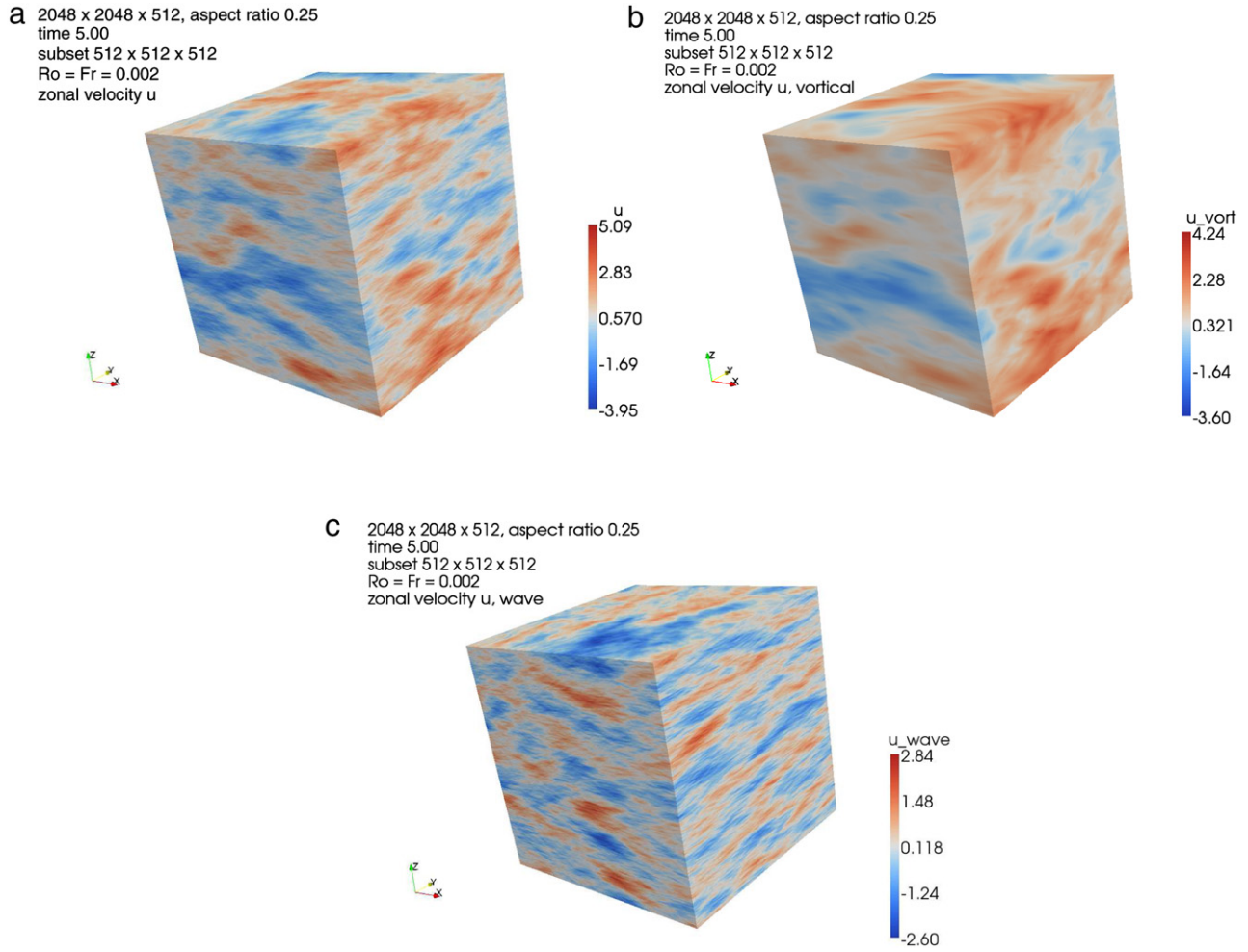


**Fig. 10.** (Color online) Run 6 ( $\delta = 0.25$ ,  $\epsilon = 0.002$ ),  $512 \times 512 \times 512$  subset showing (a) total, (b) vortical and (c) wave components of the zonal velocity.

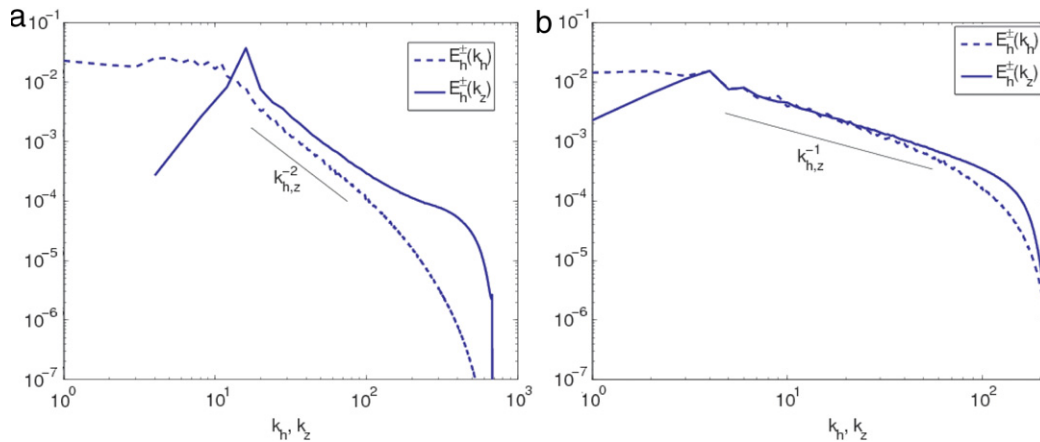


**Fig. 11.** Comparison of the wave component of horizontal kinetic energy as a function of  $k_h$  and  $k_z$  for (a) run 6,  $\delta = 0.25$  and (b) run 8,  $\delta = 1$ . Note the steeper scaling in (a) as well as the appearance of a second scaling range as a function of  $k_z$ .

It must be noted that the layered structure for  $\delta < 1$  is different from the  $k_h = 0$  wave modes (VSHF) since the contribution of those modes to the flow is insignificant. Thus, the layered structure that is often connected with the large scales in strongly stratified flows is here observed in a slightly different form. Future work will explore integral length scale measurements to characterize the differences in flow structure observed in Fig. 9 for  $\delta = 1$  and  $\delta = 1/4$ , as well as the case  $Bu = 4$  with  $\delta = 1$ . Other avenues

for future work include flow response to small-scale forcing and investigation of even smaller aspect ratios.

### Acknowledgments

We are honored to submit this manuscript to this special issue in memory of Robert. H. Kraichnan and Akiva Yaglom upon whose foundational work much of our understanding of fluid turbulence continues to rely.

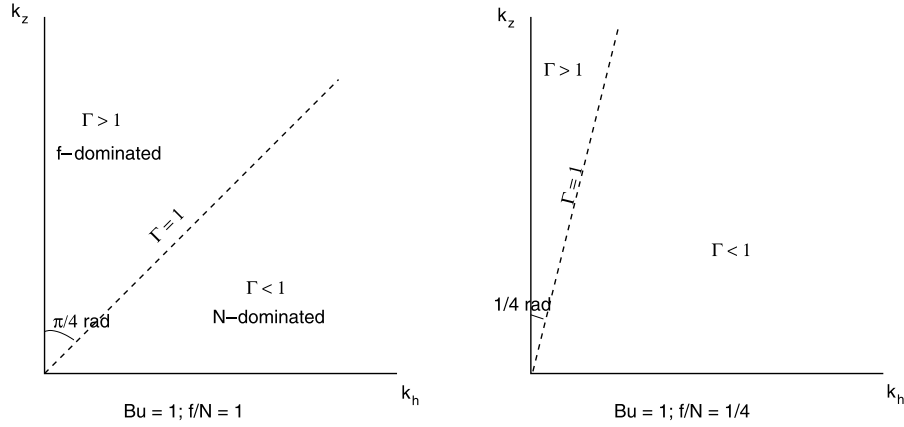


**Fig. 12.** 2d schematic of the wavenumber space in  $(k_h, k_z)$  showing the stratification and rotation dominated wavevectors as  $\Gamma$  is varied relative to  $\Gamma = 1$  for the two  $Bu = 1$  flows. On the left for  $f/N = 1$  at  $Bu = 1$ , there is an even split in wavenumber space for contributions from rotation and stratification; on the right for  $f/N = 1/4$  at  $Bu = 1$ , there is a greater contribution from stratification.

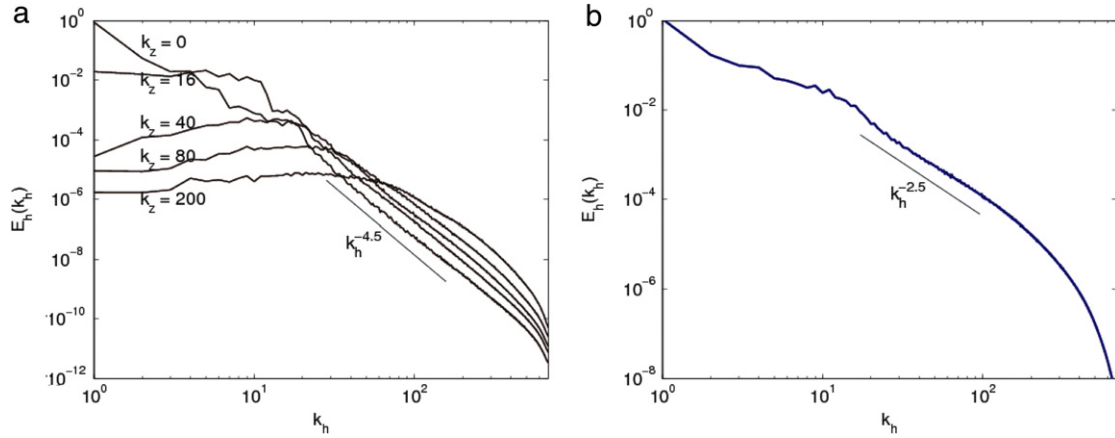


**Fig. 13.** Run 6 ( $\delta = 0.25$ ,  $\epsilon = 0.002$ ), horizontal kinetic energy  $E_h$  (a) as a function of  $k_h$  for five fixed values of  $k_z = \{0, 16, 40, 80, 200\}$ , and (b) as a function of  $k_h$  summed over all  $k_z$ .

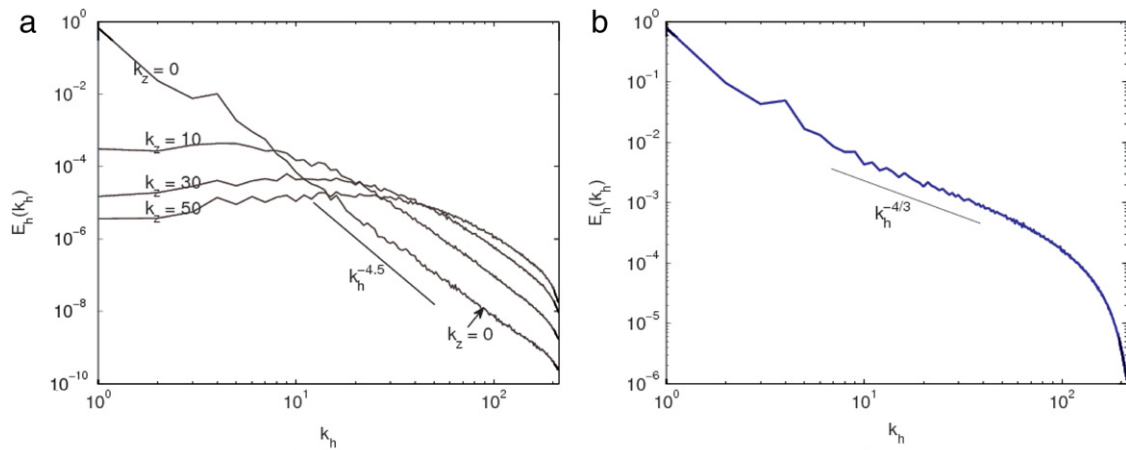


**Fig. 14.** Run 8 ( $\delta = 1$ ,  $\epsilon = 0.0023$ ), horizontal kinetic energy  $E_h$  (a) as a function of  $k_h$  for four fixed values of  $k_z = \{0, 10, 30, 50\}$ , and (b) as a function of  $k_h$  summed over all  $k_z$ .

We thank Ramesh Balakrishnan (Argonne National Laboratory), Mark A. Taylor (Sandia National Laboratories) for help in running our massive calculations, and Fabian Waleffe (University of Wisconsin, Madison) and for useful suggestions. This research used resources of the Argonne Leadership Computing Facility at Argonne National Laboratory, which is supported by the Office

of Science of the US Department of Energy under contract DE-AC02-06CH11357. Partial funding for SK was provided by the DOE Office of Science, ASCR program in Applied Mathematics. LMS received partial funding from the NSF program Collaborations in the Mathematical Geosciences: NSF CMG-1025188.

## Appendix

The eigenfunction  $\phi^+$  corresponding to  $\sigma_+$  in (3) is

$$\phi^+ = \frac{1}{\sqrt{2}\sigma k} \times \left( \frac{k_z}{k_h} (\sigma k_x + i k_y f), \frac{k_z}{k_h} (\sigma k_y - i k_x f), -\sigma k_h, -i b k_h \right) \quad (30)$$

where  $\sigma = |\sigma_{\pm}(\mathbf{k})|$ . The eigenfunction  $\phi^-$  corresponding to  $\sigma_-$  in (3) is the complex conjugate of  $\phi^+$ . The vortical mode  $\phi^0$  with zero frequency ( $\sigma_0 = 0$ ), is given by

$$\phi^0 = \frac{1}{\sigma k} (N k_y, -N k_x, 0, f b k_z / N). \quad (31)$$

Two special cases must be considered: (i)  $k_h = 0$  and (ii)  $k_z = N = 0$ . For special case (i)  $k_h = 0$ , when the wavevector is parallel to the rotation and stratification axis, orthonormal eigenfunctions satisfying continuity are

$$\phi^+ = \left( \frac{1+i}{2}, \frac{1-i}{2}, 0, 0 \right), \quad (32)$$

$$\phi^- = (\phi^+)^*, \quad \phi^0 = (0, 0, 0, b/N)$$

where  $()^*$  denotes complex conjugate. These are the vertically sheared horizontal flow modes or VSHF modes. They have no vertical vorticity and no potential vorticity. They also have no vertical velocity because of the continuity constraint  $\nabla \cdot \mathbf{u} = 0$ . The wave frequencies corresponding to  $\phi^+$  and  $\phi^-$  are, respectively,  $\sigma_+ = f$  and  $\sigma_- = -f$ . Density fluctuations represented by  $\phi^0$  have zero frequency  $\sigma_0 = 0$ . Special case (ii),  $k_z = N = 0$ , corresponds to pure rotation with wavevector perpendicular to the rotation axis. In this case, the eigenmodes are all slow (geostrophic) modes with zero frequency  $\sigma_+ = \sigma_- = \sigma_0 = 0$ , taken as

$$\phi^+ = \frac{1}{\sqrt{2}k_h} (i k_y, -i k_x, -k_h, 0), \quad (33)$$

$$\phi^- = (\phi^+)^*, \quad \phi^0 = (0, 0, 0, b/N).$$

## References

- [1] A. Gill, Atmosphere-Ocean Dynamics, in: International Geophysics Series, Academic Press, 1981.
- [2] A. Majda, Introduction to PDEs and Waves for the Atmosphere and Ocean, in: Courant Lecture Notes in Mathematics, vol. 9, New York University Courant Institute of Mathematical Sciences, New York, 2003.
- [3] G. Vallis, Atmospheric and Oceanic Fluid Dynamics, Cambridge University Press, Cambridge, 2006.
- [4] A. Kolmogorov, On degeneration (decay) of isotropic turbulence in an incompressible viscous liquid, Dokl. Akad. Nauk SSSR 31 (1941) 538–540.
- [5] R. Kraichnan, Inertial ranges in two-dimensional turbulence, Phys. Fluids 10 (1967) 1417–1423.
- [6] R. Kraichnan, Inertial-range transfer in two and three-dimensional turbulence, J. Fluid Mech. 47 (1971) 525–535.
- [7] A. Yaglom, On the local structure of a temperature field in a turbulent flow, Dokl. Akad. Nauk SSSR 69 (1949) 743–746.
- [8] P. Bartello, Geostrophic adjustment and inverse cascades in rotating stratified turbulence, J. Atmospheric Sci. 52 (1995) 4410–4428.
- [9] M. Waite, P. Bartello, Stratified turbulence dominated by vortical motion, J. Fluid Mech. 517 (2004) 281–308.
- [10] M. Waite, P. Bartello, Stratified turbulence generated by internal gravity waves, J. Fluid Mech. 546 (2006) 313–339.
- [11] M. Waite, P. Bartello, The transition from geostrophic to stratified turbulence, J. Fluid Mech. 568 (2006) 89–108.
- [12] L. Smith, F. Waleffe, Generation of slow, large scales in forced rotating, stratified turbulence, J. Fluid Mech. 451 (2002) 145–168.
- [13] J. Sukhatme, L. Smith, Vortical and wave modes in 3d rotating stratified flows: random large scale forcing, Geophys. Astrophys. Fluid Dyn. 102 (2008) 437–455.
- [14] S. Kurien, B. Wingate, M. Taylor, Anisotropic constraints on energy distribution in rotating and stratified flows, Europhys. Lett. 84 (2008) 24003.
- [15] S. Kurien, Scaling of high-wavenumber energy spectra in the unit aspect-ratio rotating Boussinesq system, J. Fluid Mech. (2011) (in preparation) arXiv:1005.5366v1 [nlin.CD].
- [16] Y. Kitamura, Y. Matsuda, The  $k_h^3$  and  $k_h^{-5/3}$  energy spectra in stratified turbulence, Geophys. Res. Lett. 33 (2006) L05809.
- [17] M. Remmel, J. Sukhatme, L. Smith, Nonlinear inertia-gravity wave-mode interactions in three-dimensional rotating stratified flows, Commun. Math. Sci. 8 (2010) 357–376.
- [18] J. Riley, R. Metcalfe, M. Weissman, Direct numerical simulations of homogeneous turbulence in density-stratified fluids, in: Nonlinear Properties of Internal Waves, AIP, 1981, pp. 79–112.
- [19] D. Lilly, Stratified turbulence and the mesoscale variability of the atmosphere, J. Atmospheric Sci. 40 (1983) 749–761.
- [20] A. Majda, M. Grote, Model dynamics and vertical collapse in decaying strongly stratified flows, Phys. Fluids 9 (1997) 2932–2940.
- [21] F. Godeferd, C. Cambon, Detailed investigation of energy transfers in homogenous stratified turbulence, Phys. Fluids 6 (1984) 2084–2100.
- [22] J. Riley, S. deBruynKops, Dynamics of turbulence strongly influenced by buoyancy, Phys. Fluids 15 (2003) 2047–2059.
- [23] J. Sukhatme, L. Smith, Self-similarity in decaying two-dimensional stably stratified adjustment, Phys. Fluids 19 (2007) 036603.
- [24] L. Smith, Numerical study of two-dimensional stratified turbulence, Contemp. Math. 283 (2001) 91.
- [25] O. Metais, J. Herring, Numerical studies of freely decaying homogeneous stratified turbulence, J. Fluid Mech. 202 (1989) 117–148.
- [26] L. Smith, F. Waleffe, Generation of slow, large scales in forced rotating, stratified turbulence, J. Fluid Mech. 451 (2002) 145–168.
- [27] J.-P. Laval, J. McWilliams, B. Dubrulle, Forced stratified turbulence: successive transitions with Reynolds number, Phys. Rev. E 68 (2003) 036308.
- [28] A. Babin, A. Mahalov, B. Nicolaenko, Y. Zhou, On the asymptotic regimes and the strongly stratified limit of rotating Boussinesq equations, Theor. Comput. Fluid Dyn. 9 (1997) 223.
- [29] E. Lindborg, The energy cascade in a strongly stratified fluid, J. Fluid Mech. 550 (2006) 207–242. doi:10.1017/S0022112005008128.
- [30] P. Embid, A. Majda, Low Froude number limiting dynamics for stably stratified flow with small or finite Rossby numbers, Geophys. Astrophys. Fluid Dyn. 87 (1–2) (1998) 1–50.
- [31] G. Brethouwer, P. Billant, E. Lindborg, J.-M. Chomaz, Scaling analysis and numerical simulations of strongly stratified turbulent flows, J. Fluid Mech. 585 (2007) 343–368.
- [32] E. Lindborg, G. Brethouwer, Stratified turbulence forced in rotational and divergent modes, J. Fluid Mech. 586 (2007) 83–108.
- [33] J. Charney, Geostrophic turbulence, J. Atmospheric Sci. 28 (1971) 1087–1095.
- [34] R. Salmon, Lectures on Geophysical Fluid Dynamics, Oxford University Press, New York, 1998.
- [35] J.C. McWilliams, P.R. Gent, Intermediate models of planetary circulations in the atmosphere and ocean, J. Atmospheric Sci. 37 (8) (1980) 1657–1678.
- [36] J. Allen, Iterated geostrophic intermediate models, J. Phys. Oceanogr. 23 (1) (1993) 2447–2461.
- [37] J. Allen, P. Newberger, On intermediate models for stratified flow, J. Phys. Oceanogr. 23 (2) (1993) 2462–2485.
- [38] D. Muraki, C. Snyder, R. Rotunno, The next-order corrections to quasi-geostrophic theory, J. Atmospheric Sci. 56 (1999) 1547–1560.
- [39] M. McIntyre, W. Norton, Potential vorticity inversion on a hemisphere, J. Atmospheric Sci. 57 (9) (2000) 1214–1235.
- [40] M. Remmel, L. Smith, New intermediate models for rotating shallow water and an investigation of the preference for anticyclones, J. Fluid Mech. 635 (2009) 321–359.
- [41] G. Nastrom, K. Gage, A climatology of atmospheric wavenumber spectra of wind and temperature observed by commercial aircraft, J. Atmospheric Sci. 42 (1985) 950–960.
- [42] E. Spiegel, G. Veronis, On the Boussinesq approximation for a compressible fluid, Astrophys. J. 131 (1960) 442–447.
- [43] J.R. Chasnov, Similarity states of passive scalar transport in isotropic turbulence, Phys. Fluids 6 (2) (1994) 1036–1051.
- [44] U. Frisch, S. Kurien, R. Pandit, W. Pauls, S.S. Ray, A. Wirth, J.-Z. Zhu, Hyperviscosity, galerkin-truncation and bottlenecks in turbulence, Phys. Rev. Lett. 101 (2008) 144501.
- [45] T. Gotoh, D. Fukayama, T. Nakano, Velocity field statistics in homogeneous steady turbulence obtained using a high-resolution direct numerical simulation, Phys. Fluids 14 (2002) 1065–1081.
- [46] M. Taylor, S. Kurien, G. Eyink, Recovering isotropic statistics in turbulence simulations: the Kolmogorov 4/5th law, Phys. Rev. E 68 (2003) 026310.